

Detection of CO and HCN in Pluto's atmosphere with ALMA

E. Lellouch¹, M. Gurwell², B. Butler³, T. Fouchet¹, P. Lavvas⁴, D.F. Strobel⁵, B. Sicardy¹, A. Moullet⁶, R. Moreno¹, D. Bockelée-Morvan¹, N. Biver¹, L. Young⁷, D. Lis⁸, J. Stansberry⁹, A. Stern⁷, H. Weaver¹⁰, E. Young⁷, X. Zhu¹⁰, J. Boissier¹¹

¹ *LESIA, Observatoire de Paris, PSL Research University, CNRS, Sorbonne Universités, UPMC Univ. Paris 06, Univ. Paris Diderot, Sorbonne Paris Cité, 5 place Jules Janssen, 92195 Meudon, France; emmanuel.lellouch@obspm.fr*

² *Harvard-Smithsonian Center for Astrophysics, Cambridge, MA 02138, USA*

³ *National Radio Astronomy Observatory, Socorro, NM 87801, USA*

⁴ *GSMA, Université Reims Champagne-Ardenne, 51687 Reims Cedex 2, France*

⁵ *Department of Earth and Planetary Sciences and Physics and Astronomy, Johns Hopkins University, Baltimore, MD 21218, USA*

⁶ *National Radio Astronomy Observatory, Charlottesville, VA 22902, USA*

⁷ *Southwest Research Institute, Boulder, CO 80302, USA*

⁸ *LERMA, Observatoire de Paris, PSL Research University, CNRS, Sorbonne Universités, UPMC Univ. Paris 06, 75014 Paris, France*

⁹ *Space Telescope Science Institute, Baltimore, MD 21218, USA*

¹⁰ *Space Exploration Sector, Applied Physics Laboratory, Johns Hopkins University, Laurel, MD 20723, USA*

¹¹ *IRAM, 38400 Saint-Martin-d'Hères, France*

Abstract

Observations of the Pluto-Charon system, acquired with the ALMA interferometer on June 12-13, 2015, are presented. A highlight of these observations is the detection of the CO(3-2) and HCN(4-3) rotational transitions from Pluto (including the hyperfine structure of HCN) providing a strong confirmation of the presence of CO, and the first observation of HCN in Pluto's atmosphere. The CO and HCN lines probe Pluto's atmosphere up to ~ 450 km and ~ 900 km altitude, respectively, with a large contribution due to limb emission. The CO detection yields (i) a much improved determination of the CO mole fraction, as 515 ± 40 ppm for a $12 \mu\text{bar}$ surface pressure (ii) strong

constraints on Pluto’s mean atmospheric dayside temperature profile over ~ 50 -400 km, with clear evidence for a well-marked temperature decrease (i.e., mesosphere) above the 30-50 km stratopause and a best-determined temperature of 70 ± 2 K at 300 km, somewhat lower than previously estimated from stellar occultations (81 ± 6 K), and in agreement with recent inferences from New Horizons / Alice solar occultation data. The HCN line shape implies a high abundance of this species in the upper atmosphere, with a mole fraction $> 1.5 \times 10^{-5}$ above 450 km and a value of 4×10^{-5} near 800 km. Assuming HCN at saturation, this would require a warm (> 92 K) upper atmosphere layer; while this is not ruled out by the CO emission, it is inconsistent with the Alice-measured CH_4 and N_2 line-of-sight column densities. Taken together, the large HCN abundance and the cold upper atmosphere imply supersaturation of HCN to a degree (7-8 orders of magnitude) hitherto unseen in planetary atmospheres, probably due to a lack of condensation nuclei above the haze region and the slow kinetics of condensation at the low pressure and temperature conditions of Pluto’s upper atmosphere. HCN is also present in the bottom ~ 100 km of the atmosphere, with a 10^{-8} - 10^{-7} mole fraction; this implies either HCN saturation or undersaturation there, depending on the precise stratopause temperature. The HCN column is $(1.6 \pm 0.4) \times 10^{14} \text{ cm}^{-2}$, suggesting a surface-referred vertically-integrated net production rate of $\sim 2 \times 10^7 \text{ cm}^{-2} \text{ s}^{-1}$. Although HCN rotational line cooling affects Pluto’s atmosphere heat budget, the amounts determined in this study are insufficient to explain the well-marked mesosphere and upper atmosphere’s ~ 70 K temperature. We finally report an upper limit on the HC_3N column density ($< 2 \times 10^{13} \text{ cm}^{-2}$) and on the $\text{HC}^{15}\text{N} / \text{HC}^{14}\text{N}$ ratio ($< 1/125$).

Keywords: Pluto; Pluto, atmosphere

1. Introduction

Ground-based and New Horizons observations have shown Pluto's tenuous, N₂-dominated, atmosphere to be alluringly Mars- and Titan- like. The long-term monitoring of stellar occultations (Elliot et al., 2003; Sicardy et al., 2003; Olkin et al., 2015; Sicardy et al., 2016, and references therein) has revealed a factor-of-three pressure increase in the last 25 years, with a current pressure in the range $\sim 10\text{-}14 \mu\text{bar}$ (Gladstone et al., 2016; Sicardy et al., 2016). This variability reflects the existence of Mars-like seasonal cycles, in which volatiles, CH₄ and CO in addition to N₂ (Owen et al., 1993; Douté et al., 1999; Grundy et al., 2013), are shared between atmospheric and surface ice reservoirs through sublimation/condensation exchanges and migration (Young, 2013; Hansen et al., 2015; Olkin et al., 2015). Most spectacularly, New Horizons discovered a thick ice cap at low latitudes (informally named Sputnik Planum) as being the main reservoir of volatiles, in addition to thinner N₂ frosts at mid-northern latitudes and more widespread CH₄ frost (Stern et al., 2015; Grundy et al., 2016).

Near-infrared spectroscopy (Young et al., 1997; Lellouch et al., 2009, 2015a) revealed CH₄ as the second most abundant atmospheric species ($\sim 0.5\%$ of N₂), providing an explanation for the relatively warm stratosphere ($\sim 105\text{-}110\text{ K}$ at 20-50 km altitude compared to $\sim 35\text{-}55\text{ K}$ at the surface). Similar to Titan, the coupled photochemistry of N₂ and CH₄ is expected to result in the production of a suite of minor species, including hydrocarbons and nitriles (Lara et al., 1997; Summers et al., 1997; Krasnopolsky and Cruikshank, 1999; Gladstone et al., 2015) and ultimately haze formation. Several hydrocarbons (C₂H₂, C₂H₄ and C₂H₆) were indeed detected by the New Horizons UV experiment (Gladstone et al., 2016). Most impressively, extensive, optically thin hazes are seen in New Horizons images, extending to altitudes of $>200\text{ km}$, with a distinctly layered structure that may be the sign of gravity wave activity, evidence for which is also present in stellar occultation data (e.g. Toigo et al., 2015). Other key atmospheric results from New Horizons include detailed temperature profiles below 50 km, and evidence for a cold upper atmosphere ($\sim 70\text{ K}$ above 500 km) which effectively limits the escape rate of Pluto's atmosphere to space to much smaller values than anticipated.

Besides CH₄, the search for minor species in Pluto's atmosphere from the ground has proven difficult. A number of searches for CO were conducted at radio-wavelengths, but as will be detailed below, results were unconstraining (Barnes, 1993), tentative (Bockelée-Morvan et al., 2001), or erroneous in the case of Greaves et al. (2011), as demonstrated by Gurwell et al. (2014). In the near-IR, from IRTF/CSHELL observations of the CO(2-

0) band at $2.3 \mu\text{m}$, Young et al. (2001) determined a coarse upper limit to the CO column density ($< 45\text{-}130 \text{ cm-am}$, i.e. typically 20-60 % of N_2). The same spectral region was re-observed with much improved sensitivity with VLT/CRIRES (Lellouch et al., 2011). Besides the undisputable presence of CH_4 features, the spectrum showed indication for a number of CO lines, which upon co-adding, yielded evidence for CO in Pluto’s atmosphere at the 6σ level, with a 500^{+1000}_{-250} ppm mixing ratio (i.e. a $\sim 0.1 \text{ cm-am}$ column density), which within (large) error bars, was consistent with the CO: N_2 ratio in Pluto ice derived by Douté et al. (1999).

While most hydrocarbons are non-polar, nitriles exhibit strong rotational lines and are thus well suited to mm/submm searches, as demonstrated notably in the case of Titan’s atmosphere by the routine observation of HCN, HC_3N , CH_3CN and some of their isotopes, and the recent detection of ethyl cyanide ($\text{C}_2\text{H}_5\text{CN}$) and vinyl cyanide ($\text{C}_2\text{H}_3\text{CN}$) with ALMA (Cordiner et al., 2015a,b). In this paper, we report on searches for CO, HCN and HC_3N in Pluto’s atmosphere with ALMA, leading to the strong confirmation of CO and the first detection of HCN.

2. Observations and data reduction

Observations of the Pluto-Charon system were obtained with the 12-m array of the Atacama Large Millimeter Array (ALMA). This synthesis array is a collection of radio antennas, each 12 m in diameter, deployed out on the Chajnantor Plateau in the high northern Chilean Andes. Each pair of antennas acts as a two-element interferometer, and the combination of all of these individual interferometers allows for the reconstruction of the full sky brightness distribution (Thompson et al., 2001).

ALMA is currently tunable in 7 discrete frequency bands, from ~ 90 to ~ 950 GHz. Observations reported here were taken in Band 7, near 350 GHz. Scientific goals included: (i) independent measurements of continuum emission from the surfaces of Pluto and Charon and (ii) search for emission from atmospheric constituents (CO, HCN and HC_3N). To achieve these purposes, we tuned the receivers and set up the correlator in four separate frequency ranges (spectral windows) and resolutions: one “continuum” (so-called “Time Division Mode” – TDM) range, and three “spectral line” (so-called “Frequency Division Mode” – FDM) ranges. Details on the frequency ranges, spectral resolutions and targetted lines are given in Table 1.

All observations were taken in dual-linear polarization. As atmospheric line emission is not expected to be polarized, data in the two polarizations were combined to provide a measurement of the total intensity (Stokes I).

Table 1: Observation spectral set-ups.

#	Spectral range (GHz)	Resolution (MHz)	Targetted lines and frequencies (GHz)
0	354-356	15.625	Continuum
1	345.598-345.832	0.141	CO(3-2); 345.796 HC ₃ N(38-37); 345.609
2	354.380-354.849	0.282	HCN(4-3); 354.505 HC ₃ N(39-38); 354.697
3	344.011-344.949	0.488	HC ¹⁵ N(4-3); 344.200

The observations were undertaken on two separate dates, June 12 and June 13, 2015. There were 39 operating antennas in the array, in the C36-7 configuration. This configuration, which has a maximum antenna separation of ~ 800 m, yielded at these frequencies a $\sim 0.35''$ resolution (i.e., 8100 km at Pluto’s distance). This resolution is sufficient to separate the emission of Pluto from Charon, but not enough to resolve either of the bodies themselves. Table 2 provides relevant geometrical parameters for the two observing dates.

On each date, the entire observation took 1 hour 40 minutes, of which about 55 minutes were on Pluto/Charon. We observed the calibrator J1924-2914 to calibrate bandpass and delay, and Titan for absolute flux density calibration. The expected overall flux density scale accuracy is 5%, using a standard model for Titan (Butler, 2012). We used the point-like radio source J1911-2006 to calibrate the phase of the atmosphere and the antennas as a function of time, as well as temporal variations of amplitude gain; the derived flux density of this calibrator was ~ 0.75 Jy on both observing dates.

Initial calibration of the data was provided by the ALMA observatory, and done in the CASA reduction package, version 4.3.1 (Muders et al., 2014). The actual measured quantity of an interferometer like ALMA is a sampling of the complex visibility function for the baselines (length and orientation) between each of its antennas. The visibility function is the two-dimensional Fourier transform of the sky brightness distribution. The individual samples of the visibility function are referred to as visibilities, and are complex quantities (real and imaginary, or amplitude and phase). After the initial calibration, the data product was a set of visibilities for each of the observing dates.

Data acquisition with ALMA is performed with fixed frequencies. Because of this, a correction to the data must be made to account for the changing Doppler shift of Pluto/Charon with respect to ALMA. In addi-

Table 2: Observing dates and geometry.

Date	Time range (UTC)	Geocentric Distance (AU)	Sub-Earth Longitude ^a	Pluto-Charon separation (arcsec)
2015-Jun-12	04:15–05:55	31.958	157	0.70
2015-Jun-13	03:25–05:05	31.952	103	0.84

^a Sub-observer East longitude at mid-point. We adopt the new IAU convention for definition of the North Pole (Buie et al., 1997; Zangari, 2015), with current summer in the northern hemisphere. Zero longitude on Pluto is the sub-Charon point and the sub-observer point longitude decreases with time.

tion, this correction puts the frequency scale in the proper rest frame. This correction was done with the CASA tasks *fixplanets()* and *cvel()*. These tasks were run on each of the above spectral windows separately.

At this point we exported the data from CASA and continued the data reduction in the AIPS package (www.aips.nrao.edu/CookHTML/CookBook.html). We imaged the continuum spectral window, from which we used the technique of self-calibration to correct for residual phase errors (left over after the removal of the time-variable complex gain from the calibrator) in the visibilities (Cornwell and Fomalont, 1999). We did this iteratively with solution intervals of 5, 2, and 1 minute. Since the phase errors at this point are primarily due to tropospheric water vapor, and the frequency difference between the spectral windows is not large, the phase solutions found for the continuum window could be used to correct the data in the spectral line spectral windows.

Finally, we subtracted the continuum in the three spectral line windows (18.2 mJy in CO(3-2) and HC¹⁵N(4-3), and 18.9 mJy in HCN(4-3)). We did this in the visibility domain, using an average of spectral channels that were far outside the line emission region (van Langevelde and Cotton, 1990).

While no atmospheric emission was detected from Charon, the main highlight of the observations was the detection of line emission due to CO and HCN from Pluto’s atmosphere. Following preliminary reports of these data (Lellouch et al., 2015b,c; Gurwell et al., 2015), this result is the focus of the present paper. Continuum measurements have been briefly presented (Butler et al., 2015) and will be described in detail in a future publication.

3. Data assessment

Continuum-subtracted Pluto spectra in the vicinity of the CO(3-2) and HCN(4-3) lines are shown in Fig. 1 separately for the two observing dates. A strong detection of both lines was achieved on each day, providing the first detection of HCN in Pluto’s atmosphere and the first observation of CO at radio-wavelengths. The HCN spectra clearly show the hyperfine structure, with weak emission features at -1.6 and +2.0 MHz from the main line. These secondary emissions (termed hereafter the “satellite lines”) arise from transitions with very similar lower energy levels but with absolute strengths (hence opacities) are ~ 45 times weaker than the main line (which is itself the unresolved sum of three components). As shown below, these secondary lines are quite useful for constraining the HCN vertical distribution.

Data from the two different days do not show significant differences. In particular, although observations on June 12 (subearth longitude $L = 157^\circ\text{E}$) fully encompassed Sputnik Planum – centered at 20°N , 175°E and which is the region showing the largest concentration of CO ice (Grundy et al., 2016)¹ – this does not result in an enhancement of the gas CO feature. This is qualitatively consistent with expectations from recent multi-species General Climate Models that CO is well mixed with N_2 (Forget et al., 2016). Data from the two days were therefore averaged for further analysis.

The averaged CO(3-2) and HCN(4-3) line contrasts are 61 mJy and 99 mJy at $\Delta\nu = 141$ and 282 kHz resolution, respectively. With $1\text{-}\sigma$ rms residuals of 3.28 mJy and 2.85 mJy, this gives a S/N detection of 19 for CO and 35 for HCN at the peak. However, the CO and HCN line shapes are very different. The main HCN line is narrow (~ 0.8 MHz FWHM), with residual flux falling practically to zero between the main and the satellite lines. The CO line is broader (~ 2 MHz FWHM), with signal being detected up to ± 5 MHz in the wings. The S/N on the integrated line is 160 for CO and 58 for HCN.

Finally, no detection of HC_3N or HC^{15}N was achieved, with $1\text{-}\sigma$ rms residuals of 3.28 mJy at $\Delta\nu = 141$ kHz for $\text{HC}_3\text{N}(38\text{-}37)$, 2.85 mJy at $\Delta\nu = 282$ kHz for $\text{HC}_3\text{N}(39\text{-}38)$ and 1.88 mJy for $\text{HC}^{15}\text{N}(4\text{-}3)$ at $R = 488$ kHz.

While data-model comparisons are hereafter presented in the observational flux units, expressing the data in brightness temperature is useful for qualitative assessment and comparison with previous CO searches. With a Pluto apparent size of 0.103 arcsec, the CO line contrast of 61 mJy, su-

¹ Schmitt et al. (2016) report that CO ice is also present at mid-northern latitudes in Venera Terra and Burney crater.

perimposed to a 18.2 mJy continuum, translates into a 119 K brightness temperature (T_B) at the peak, and a 85 K Rayleigh-Jeans temperature contrast (ΔT_{RJ}) with respect to the continuum. For HCN, the 99 mJy contrast, superimposed to 18.9 mJy continuum, indicates a peak $T_B = 165$ K and $\Delta T_{RJ} = 132$ K. The fact that the peak T_B are higher than Pluto’s stratopause temperature directly implies that a significant fraction of the emission originates from limb viewing (i.e. rays not intercepting the surface), enhancing the size of Pluto’s emitting disk.

Based on IRAM-30 m observations in April 2000, Bockelée-Morvan et al. (2001) reported a tentative detection of the CO(2-1) line, with an integrated line area of (18 ± 4) mK-MHz and a ~ 15 mK main-beam temperature contrast. With a 10.6 arcsec half-power beam width (HPBW) of the telescope at CO(2-1) and a Pluto $0.111''$ apparent size at the time, this line contrast would have corresponded to a $\Delta T_{RJ} = 196$ K contrast at Pluto. This is inconsistent with $\Delta T_{RJ} = 85$ K that we measure for CO(3-2) (all the more so when considering that CO(3-2) is also intrinsically stronger than CO(2-1)), implying that the possible line reported by the authors, but wisely treated as an upper limit, was not real. Similarly but more detrimental for what was published as a “discovery”, the claimed, yet unmodelled, detection of CO(2-1) by Greaves et al. (2011) from JCMT, with a line contrast >4 larger (i.e., ~ 800 K contrast) than that in Bockelée-Morvan et al. (2001), was undoubtedly spurious. Note that based on a deep search (17 hours integration) for CO(2-1) with the SMA, Gurwell et al. (2014) reported no detection while reaching a 82 mJy rms at 100 kHz resolution; as such this was already enough to refute the Greaves et al. (2011) results at $10\text{-}\sigma$ confidence.

4. Modelling and analysis

To analyze the data, we developed our own standard radiative transfer code, fully accounting for the spherical geometry associated with the large extent of Pluto’s atmosphere compared to the object’s radius. Line opacities for CO and HCN were calculated using line parameters from the Cologne database (Müller et al., 2011), including the hyperfine structure for HCN. Collisional broadening by N_2 were taken from Koshelev and Markov (2009), Priem et al. (2000) and Yang et al. (2008), giving HWHM’s of 2.14 and 4.20 GHz/bar at 300 K for CO(3-2) and HCN (4-3), with temperature exponents of -0.84 and -0.69 respectively. Emission from the surface was calculated by using a Fresnel-emission model with a dielectric constant of 3.5, adjusting the surface temperature to match the measured contin-

uum flux ($T_{surf} = 38.0$ K and 38.4 K for CO and HCN respectively)². Atmospheric pressure-temperature-altitude profiles were calculated using a molecular mass of 27.94 to account for the presence of CH₄ in Pluto’s atmosphere. The altitude variation of the gravity was accounted for, using a surface radius of 1190 km based New Horizons/REX (Gladstone et al., 2016). A surface pressure of 12 μ bar was nominally assumed, intermediate between values inferred from the June 29, 2015 stellar occultation (11.9–13.7 μ bar, Sicardy et al., 2016) and from the New Horizons/REX (11 ± 1 and 10 ± 1 μ bar at entry and exit, respectively, Gladstone et al., 2016). As discussed below we also considered values of 10 and 14 μ bar. Contributions to the emission of the individual (vertical and horizontal) lines-of-sight were calculated as a function of distance D from Pluto’s center (using geometrically exact pathlengths in each layer) for $0 \text{ km} < D < 2500 \text{ km}$ and convolved with the synthetic beam of the array (although this was a minor effect given the $\sim 0.35''$ HPBW, compared to $\sim 0.15''$ for Pluto’s diameter at 600 km altitude) and finally co-added.

Local thermodynamical equilibrium (LTE) was assumed throughout the atmosphere when calculating the HCN / CO rotational populations and performing the radiative transfer calculations. The de-excitation coefficient for the HCN(4-3) transition by collisions with N₂ can be estimated to $2.2\times 10^{-11} \text{ cm}^3\text{s}^{-1}$ at 30-100 K. This value comes from (i) an excitation coefficient of $9\times 10^{-12} \text{ cm}^3\text{s}^{-1}$ for HCN(4-3) by He (Dumouchel et al., 2010)³ (ii) its scaling by a factor 3.1 to obtain the excitation rate by N₂, following Rezac et al. (2013) (iii) the application of detailed balance relating excitation and de-excitation coefficients. With an Einstein coefficient $A = 2.05\times 10^{-3} \text{ s}^{-1}$, rotational LTE is ensured for HCN(4-3) up to a critical density of $9.3\times 10^7 \text{ cm}^{-3}$, i.e. a pressure of 9×10^{-13} bar. In Pluto’s atmosphere this is reached at an altitude of ~ 1150 km, where as we show below, the contribution to the total HCN emission is very small. For CO(3-2), due primarily to an Einstein coefficient 820 times weaker (and a de-excitation coefficient ~ 2 times stronger), the LTE domain extends even much higher.

4.1. CO and temperature retrievals

4.1.1. Method

The CO line contrast and shape depend on both the CO mole fraction and Pluto’s mean temperature profile. In all our retrievals, we assumed

²Other combinations of dielectric constant and surface temperature are possible, with no impact on the atmospheric results.

³See <http://basecol.obspm.fr>.

that CO is vertically uniformly mixed. This assumption is supported by (i) the absence of gravitational separation between N₂ and CO and (ii) the stability of CO against photolysis. Note also that general circulation models indicate that CO is horizontally and vertically well mixed with N₂ (Forget et al., 2016). For temperature retrieval we used a constrained and regularized algorithm following methods detailed in Conrath et al. (1998) and Rodgers et al. (2000), see also Fouchet et al. (2016) for a recent application. In this approach, temperature profiles are initialized to an a priori profile, and are constrained to stay close to this a priori at levels where the measurements contain no information. In pressure regions where information is available, the departure from the a priori profile is regularized (i.e. smoothed to some vertical resolution) to avoid spurious oscillations of the output profiles. In practice we set the correlation matrix \mathbf{S} to be a gaussian function with a correlation length equal to the atmospheric scale height. As the inversion process involves a linearization of the radiance with respect to temperature⁴, it is an iterative process. Starting from an initial temperature profile \mathbf{T} (n levels), the inversion process returns a vector $\Delta\mathbf{T}$ which must be added to \mathbf{T} for next iteration, and is given by:

$$\Delta\mathbf{T} = \mathbf{U}\Delta\mathbf{I}$$

$$\text{where } \mathbf{U} = \alpha\mathbf{S}\mathbf{K}^T(\alpha\mathbf{K}\mathbf{S}\mathbf{K}^T + \mathbf{E})^{-1}$$

Here $\Delta\mathbf{I}$ is the difference between the observed and modelled spectral radiances (m values). \mathbf{K} is the Jacobian matrix, i.e. the $m \times n$ matrix of derivatives of the radiances with temperatures $K_{ij} = dI_i/dT_j$ where I_i is the radiance at frequency i and T_j is the temperature at level j . α is a weighting factor and \mathbf{E} , the error covariance matrix of the measurements, is simply taken as a diagonal matrix with all non-zero elements equal to the square of the uncertainty of the measured radiance. Iterations were performed until convergence – defined by the constancy of the fit quality (rms between observations and models) within 1 % from an iteration to the next one – was reached.

As explained e.g. in Rodgers et al. (2000) and Fouchet et al. (2016), the information content (in terms of sounded altitude and vertical resolution) is characterized by the averaging kernels $n \times n$ matrix \mathbf{A} , defined by $\mathbf{A} = \mathbf{U}\mathbf{K}$, which contains the partial derivatives of the retrieved state with respect to

⁴For practical simplicity, the Jacobian matrix \mathbf{K} was calculated by taking into account only the derivative of the Planck function with temperature

the true state vector (here, the temperature profile). In particular, the sum of all values in a given row k of matrix \mathbf{A} is an indicator of the relative weight of the measurements and of the a priori in determining the temperature at level k , and the number of independent temperatures that can be overall retrieved from the data is given by $\text{Tr}(\mathbf{A}) = \sum_{i=1}^n A_{ii}$ (Rodgers et al., 2000, see pp. 30-31 and 46-47).

In a first step, we inverted the CO line with a fixed CO mole fraction of 500 ppm, the central value suggested by Lellouch et al. (2011). Since the observed CO line, and particularly line wings, is also sensitive to the CO mole fraction, we then also performed simultaneous temperature/abundance retrievals. For this, we followed the formalism of Conrath et al. (1998, his Equations 20-24), though with the simplification associated with the mole fraction vertical uniformity. To calculate the derivative of the spectral radiance I_i with respect to the CO abundance, we simply calculated two spectra with CO mole fractions (q) differing by 10 %, from which $dI_i/d(\ln q)$ was inferred. As detailed hereinafter, these “fixed-CO” and “free-CO” inversion processes were run with a variety of a priori temperature profiles. In all cases, the best fit corresponded to a reduced χ^2 of ~ 0.95 over a ± 15 MHz interval centered on the CO(3-2) line frequency, demonstrating the ability of the model to reproduce the observations.

4.1.2. Results, information content and uncertainties

We started with the nominal temperature profile derived from stellar occultations by Dias-Oliveira et al. (2015). Fig. 2 (green dashed line) clearly shows that the a priori temperature profile which exhibits a ~ 81 K temperature above 200 km, leads to an large overestimation of the line core contrast. This effect can be corrected by modifying the upper atmosphere (above 200 km) temperatures to reach an asymptotic value of 69 K, leaving the atmosphere below 200 km untouched (“cold Dias-Oliveira”, or “DO15 + 69 K” profile). The resulting profile (blue line) matches the line contrast, but the shape of the line core is not completely fit, as the model predicts weak absorptions at ± 0.4 MHz not observed in the data, which are produced in the model by too strong a thermal gradient over 100-300 km. Fixed-CO and free-CO inversions were then performed, using the original stellar occultation profile as a priori. For free-CO inversions, we specified an a priori CO mole fraction of 500 ppm, checking that results (i.e. the output thermal profile and CO mole fraction) were independent on this assumption. In both cases, the inversion process returns a temperature of ~ 65 K at 350 km, progressively relaxing towards the a priori at higher altitudes. In addition, the

returned temperature profile is colder than the a priori over 50-200 km, by up to 5-10 K. The fit improvement over the “cold Dias-Oliveira” profile is at the 4σ level. When the CO mole fraction was left as a free parameter, the inversion process returned a 507 ± 21 ppm value. The associated CO column density is (0.099 ± 0.004) cm-am. In vertical viewing (disk center) and at line center, the total optical depth τ is equal to 119 and the $\tau = 1$ level is reached at 300 km. In the linewings, unit optical depth at the surface is reached at ± 1.2 MHz from line center.

We extended these retrievals by using several alternative a priori profiles, namely: (i) the “standard” profile derived from New Horizons (see Fig. 3 from Gladstone et al., 2016), which combines results from Alice (above 200 km) and REX (below 60 km) with expectations based on radiative-convective thermal and diffusion models for N_2/CH_4 (ii) isothermal profiles at 50 K, 70 K and 100 K. Although these uniform profiles are obviously not realistic given pre-existing knowledge of Pluto’s atmosphere, they provide useful “end-member” cases to assess the robustness of the results. Results are given in Table 3 and Fig. 3.

Despite the large diversity of a priori profiles, all retrieved thermal profiles consistently show a common feature, namely a steady temperature decrease over at least 100-350 km. For the two most plausible a priori profiles, the stellar occultation and the New Horizons observations, the range of altitude with negative temperature gradient extends over ~ 30 -400 km. Temperatures over 250-400 km are particularly stable against a change of a priori, with a best determined temperature of 70 ± 2 K at 300 km, in full agreement with the New Horizons / Alice evidence for a cold upper atmosphere. The other strongly robust result is the determined CO mole fraction in the “CO-free retrievals”, which for the five a priori considered, varies from 474 ± 25 ppm to 523 ± 20 ppm. Restricting ourselves to the two most realistic a priori profiles, the choice of the a priori induces a $\pm 1.5\%$ uncertainty about a central 515 ppm value.

These results are in line with expectations on the information content based on examination of the averaging kernels. Averaging kernels at 0, 100, 200, 300, 500 and 700 km are shown in Fig. 4. The typical width of these kernels, 200 km, is an estimate of the vertical resolution. The peak altitude of these kernels extends up ~ 350 km, indicating that the information content decreases above this level. The total kernel (i.e. the sum of all values in a given row of the averaging kernel matrix) as a function of altitude exceeds 0.8 over 170-380 km, indicating the clear dominance of the measurements themselves over the a priori in constraining the temperatures there. The number of independent temperature measurements, as estimated from the

trace of the averaging kernel matrix, is ~ 2.5 .

Errors on the retrieved temperature profile and CO abundance resulting from random noise in the measurements are quantified in the inversion method (see Equations 23 and 24 in Conrath et al., 1998). These random temperature errors are of order 1-1.5 K over 100-400 km, progressively decreasing to smaller values (e.g. 0.5 K at the ground and at 500 km) outside of the region best constrained by the measurements. Naturally, outside of these regions, the true uncertainties are dominated by the a priori errors. Additional systematic errors originate from (i) the uncertainty in surface pressure (ii) the flux scale accuracy of the measurements (5 %). To investigate those, and starting from a “mixed” a priori profile (defined as some weighted mean of the Dias-Oliveira et al. (2015) and Gladstone et al. (2016) profile, where the relative weight of the latter increases with altitude), we re-ran the inversion process with surface pressures of 10, 12 and 14 μbar and the nominal data calibration. Additionally, for the 12 μbar case, we considered the effect of multiplicative factors of 0.95 and 1.05 on the data. Results are given in Table 3 for the CO abundance and in Fig. 5 for the temperature. The $\pm 5\%$ calibration uncertainty results in a typical ± 2 K temperature uncertainty, while the effect of surface pressure on the retrieved temperatures is smaller. Conversely (Table 3), the $\pm 5\%$ calibration uncertainty induces a $\pm 6\%$ error bar on the CO mole fraction, but the effect of surface pressure is much larger: the retrieved CO mole fraction essentially scales as $1/p_{surf}^{1.9}$. The large surface pressure dependence is due to the line saturation regime, which is partly alleviated by the increase of the line width with increasing pressure. In summary, for a fixed surface pressure, error bars on the CO mole fraction and the CO column density due to the choice of the a priori, measurement errors and calibration uncertainty amount to 1.5 %, 4 %, and 6 %, respectively, giving a global (quadratically-summed) uncertainty of 7.5 %. We conclude that the CO mole fraction in Pluto’s atmosphere is 515 ± 40 ppm for $p_{surf} = 12 \mu\text{bar}$, and must be scaled by $(12 \mu\text{bar}/p_{surf})^{1.9}$ for other adopted values of p_{surf} . The surface-referred column density⁵ is $(2.69 \pm 0.21) \times 10^{18} \text{ mol cm}^{-2}$ ($0.100 \pm 0.008 \text{ cm-am}$) for $p_{surf} = 12 \mu\text{bar}$, and scales as $(12 \mu\text{bar}/p_{surf})^{0.9}$.

⁵Throughout the paper, to account for Pluto’s sphericity, we use column densities referred to the surface, i.e. calculated as $\int N(z)(1+z/R_{pl})^2 dz$, where z is altitude, R_{pl} is Pluto radius and $N(z)$ is the gas concentration at altitude z .

Table 3: Retrieved CO abundance vs model assumptions

p_{surf} (μbar)	A priori T(z) profile	Calibration factor	CO mole fraction (ppm)	CO column density (cm-am)
12	Isothermal 50 K	1.00	474 \pm 25	0.091 \pm 0.005
12	Isothermal 70 K	1.00	486 \pm 25	0.093 \pm 0.005
12	Isothermal 100 K	1.00	514 \pm 26	0.098 \pm 0.005
12	Gladstone et al. (2016)	1.00	523 \pm 20	0.101 \pm 0.004
12	Dias-Oliveira et al. (2015)	1.00	507 \pm 21	0.099 \pm 0.004
12	Mixed	1.00	510 \pm 20	0.099 \pm 0.004
14	Mixed	1.00	388 \pm 15	0.088 \pm 0.004
10	Mixed	1.00	720 \pm 31	0.117 \pm 0.005
12	Mixed	1.05	542 \pm 21	0.105 \pm 0.005
12	Mixed	0.95	482 \pm 19	0.094 \pm 0.004

4.2. HCN results

4.2.1. Choice of temperature profile

To analyze the HCN data, we must first select a temperature profile among those fitting the CO line. As is clear from Figs. 3 and 4, there is significant latitude in this respect in the lower atmosphere (<100 km), where the retrieved thermal profile from CO is strongly influenced by the a priori. Unfortunately, the New Horizons standard profile (Gladstone et al., 2016) and the stellar occultation profile (Dias-Oliveira et al., 2015) show noticeable differences there. The former, which follows closely the REX profiles in the first 50 km, has a much less steep gradient than the latter over 0-20 km, and as we will show later (Section 5.1.2), would produce stellar occultation lightcurves markedly different from the observed. In this situation, we adopted as nominal profile the one retrieved from CO using the above “mixed” thermal profile as a priori (red line in Fig. 5). We also briefly studied the effect of using instead the “cold Dias-Oliveira” profile, which, although not optimized, led to an only slightly worse fit of the CO line. Given that the two profiles have different maximum temperatures (106 K and 110 K, respectively), this permitted us to study the impact of the stratopause temperature on the HCN results.

4.2.2. HCN initial fits

Simple hand-fitting of the HCN line using the nominal temperature profile revealed a few basic characteristics of the HCN distribution (Fig. 6). First, the narrowness of the HCN features (with no visible Lorentzian wings)

and the near-zero emission level between the HCN main line and the two satellite lines exclude a uniform distribution of HCN gas in Pluto’s atmosphere. For example, a constant $\text{HCN} = 10^{-7}$ mole fraction (red dashed-dotted line), while strongly under-estimating the main line contrast, clearly overpredicts the satellite lines and produces undesired line wings. Second, we considered an HCN profile following local saturation for solid-vapor equilibrium, using for that purpose the HCN vapor pressure vs temperature dependence provided by Fray and Schmitt (2009). Such a profile (green, long-dashed) is also strongly inadequate, especially underpredicting both the main and the satellite lines. Because the HCN vapor pressure is such a sensitive function of temperature, and our temperature retrievals have a global precision/accuracy of a few degrees, we next investigated the effect of enhancing the temperatures by +2 K when calculating the HCN vapor pressure. This case (shown in Fig. 6 as the pink dotted line) does match the contrast of the satellite lines, but continues to underpredict the main line (and overestimates the residual level in-between). Pursuing the exploration of HCN profiles with simple altitude dependence, we considered the case of uniform HCN distribution (with a q_0 mole fraction above some limiting altitude z_0 , and zero HCN at deeper levels. A rather satisfactory fit of the entire HCN spectrum (matching, in particular, the relative contrast of the main and satellite lines) was obtained for $z_0 = 460$ km and $q_0 = 4 \times 10^{-5}$, corresponding to a column density referred to Pluto’s surface of $1.3 \times 10^{14} \text{ cm}^{-2}$. Note however that this model solution produces a zero flux minimum in-between the main and satellite HCN lines, while the data marginally indicate non-zero residual flux there. This residual flux, if real, does suggest that some of the emission originates from the atmosphere below 100 km. At this stage, we obtained an optimum manual fit of the HCN spectrum (solid light blue line in Fig. 6) with a two-component HCN distribution combining (i) a lower-atmosphere component, calculated as saturated HCN for the adopted temperature profile (with a 106 K stratopause) (ii) a uniform HCN layer with $q_0 = 1.5 \times 10^{-5}$ above $z_0 = 450$ km altitude. This two-component HCN profile has a surface-referred column density of $2.0 \times 10^{14} \text{ cm}^{-2}$ (0.47×10^{14} and $1.53 \times 10^{14} \text{ cm}^{-2}$ for the upper and lower atmosphere components, respectively). In this favored model, the opacity at the main HCN line center and in vertical viewing is 3.8 (with relative contributions of 1.2 and 2.6 for the upper and lower layer respectively), and the total vertical opacity in the satellite lines is equal to 0.10.

Results in terms of HCN content and vertical distribution are very similar if the “cold Dias-Oliveira” temperature profile is used instead. In Fig. 6, we additionally show the best fit “two-component” distribution in this case.

The total HCN column density is $1.9 \times 10^{14} \text{ cm}^{-2}$. The upper atmospheric component is identical to the one found for the nominal thermal profile. The only important difference is in the interpretation of the lower atmospheric component. For this thermal profile, this component corresponds to HCN saturation at temperatures 5 K colder than prescribed by the profile, equivalent to a factor of 8 undersaturation. Thus, depending on the precise temperature in the stratopause region, we infer that HCN is either at saturation (for a stratopause at 106 K), or undersaturated by up to one order of magnitude if the stratopause is warmer.

4.2.3. HCN retrievals

We also performed some inversion retrievals of the HCN profile, returning to the nominal thermal profile (Fig. 7). Given that the hyperfine lines are optically thin and that even the main line is only moderately thick, one can expect non-unique solutions to appear in the inversion process. Such efforts are nonetheless valuable to assess the information content of the HCN observations. Starting with a vertically constant a priori profile with $\text{HCN} = 1 \times 10^{-5}$, the retrieved profile (Fig. 7, red solid line) confirms the need for sharp decrease of HCN with decreasing altitude, from $\sim 5 \times 10^{-5}$ at 800 km down to less than 10^{-7} below 150 km. In this case, the HCN mole fraction above 150 km altitude is enhanced by > 6 -7 orders of magnitude above the saturation value. Similar HCN profiles are returned for various a priori values of the HCN mole fraction (retrievals are also shown in Fig. 7 for initial $\text{HCN} = 1 \times 10^{-6}$ and 3×10^{-5}). Note that all of these profiles have significant HCN content over 200-400 km ($\text{HCN} = 1 \times 10^{-8} - 1 \times 10^{-6}$) while the manual fits in the previous subsection indicated that solutions can be also found for negligible HCN amounts in this region. We therefore tested yet another a priori, in which the HCN input profile is the sum of a constant 1×10^{-5} mole fraction above $z_0 = 470$ km and, below this altitude, of a saturated profile at a temperature 2 K higher than that of the nominal profile. While the a priori profile has a HCN mole fraction of $\sim 3 \times 10^{-7}$ at the stratopause, the inversion process returns a $\sim 2 \times 10^{-8}$ mole fraction there (green curves in Fig. 7). This confirms that the contrast of the HCN satellite lines and the residual levels between them and the main line provide an upper limit to the HCN “stratospheric” mole fraction.

Averaging kernels for HCN are shown in Fig. 8, for the profile returned with a constant 1×10^{-5} a priori mole fraction. They clearly show the two altitude regimes probed by the HCN transition (i) the 600-800 km range, probed in the main line and (ii) the lower atmosphere at 50-150 km, probed in the satellite lines.

The number of independent measurements, as given by the trace of the averaging kernel matrix, is ~ 1.5 . In fact, the data constrain rather well the HCN mole fraction to be $\sim 4 \times 10^{-5}$, over 600-800 km, and as explained above, puts a limit on the amount of HCN in the near-surface (< 100 km) atmosphere. Somehow ironically, these are the ranges where the temperature is the least well determined from the CO line. The HCN column density indicated by these retrievals is in the range $(1.2-1.4) \times 10^{14} \text{ cm}^{-2}$.

4.2.4. Evidence for HCN supersaturation and search for alternate solutions

The above manual fits and retrievals both indicate that for the nominal and alternative thermal profiles based on the CO line, the HCN line data imply a huge (> 7 orders of magnitude at 800 km) supersaturation of HCN, at least in Pluto's upper atmosphere (> 500 km), over expectations based on the Fray and Schmitt (2009) expression for the HCN vapor pressure. As vapor pressure measurements against which this expression can be verified are not available at temperatures below 230 K, its applicability down to ~ 70 K (i.e. over > 10 orders of magnitude in pressure) might seem highly hazardous. However, in addition to the vapor pressure, the heat capacity of solid HCN has been measured from 15 K to the triple point at ~ 260 K, from which that of the gas can be calculated. This approach, on which the Fray and Schmitt (2009) saturation law is based, has been validated by the authors on several other atoms and molecules (e.g Ar, CO₂) over wide pressure-temperature ranges (up to 15 orders of magnitude in pressure). This leads the authors (B. Schmitt and N. Fray, priv. comm.) to believe that uncertainties on the HCN pressure curve should not be larger than a factor of a few (typically 2-5) over $T = 65 - 100$ K. Therefore, they cannot be the cause of the apparently highly supersaturated HCN abundances, and further investigations are warranted.

An obvious way to alleviate the requirement for HCN supersaturation is to invoke a warm region in the upper atmosphere in which HCN would be concentrated. Although the latter is not naturally indicated by the CO retrievals, such a warm region might not be inconsistent with the CO line given that the latter is weakly sensitive to temperatures above 450 km. Starting from our nominal thermal profile, we explored a suite of temperature changes above 150 km, requiring that HCN is at saturation throughout the atmosphere. This specific assumption is the one that minimizes the required temperature increment in the warm layer (hence causing the least impact to the CO line). A complication in this exercise is that the lower atmosphere (< 100 km) significantly contributes to the HCN emission. For example, Fig. 6 (green line) shows that for our nominal thermal profile, a

Table 4: Temperature profiles for non-supersaturated HCN profiles

z_1 (mesopause altitude, km)	Δz_2 (warm layer thickness, km)	Mesopause temp. T_1 (K)	Warm layer temp. T_2 (K)
300	100	57	98
500	100	60	96
700	100	50	94.5
300	200	56	96.5
500	200	60	94.5
700	200	50	93.5
300	400	56	93.5
500	400	60	92.5
700	400	50	92

saturated HCN profile can account for approximately half of the HCN emission, both in the main and satellites lines. With that in mind, and keeping the temperature and HCN profiles fixed below 150 km, we explored thermal profiles characterized by (i) the altitude (z_1) and (ii) temperature (T_1) of the temperature minimum (mesopause) (iii) the temperature (T_2) and (iv) thickness (Δz_2) of the warm layer. In all the models, the base of the warm layer was located 50 km above z_1 , and the temperature above the top of the warm layer progressively returned to the nominal upper atmosphere temperature (68 K) within another 50 km. In practice, we tested three values of z_1 (300, 500, and 750 km) and three values of Δz_2 (100, 200 and 400 km), and searched for best fits of the HCN and CO lines in terms of T_1 and T_2 . Note that these temperature profiles are purely empirical, i.e. we do not examine the physical processes that could possibly drive them. Given the sharp sensitivity of the HCN vapor pressure with temperature, T_2 can be determined to within less than 1 K, while T_1 , required to maintain a good fit of CO, is determined somewhat more loosely. Results are summarized in Table 4 and Fig. 9 shows resulting fits along with the temperature and HCN profiles in the $\Delta z_2 = 200$ km case.

As is clear from Fig. 9, satisfactory solutions to the problem exist for $z_1 = 500$ and 700 km, and to a lesser extent for $z_1 = 300$ km as well. The associated temperatures of the warm layer are in the 92-98 K range, and the temperature minimum is ~ 50 -60 K. When $z_1 = 300$ km, the agreement deteriorates, as the rapid temperature increase over 300-350 km, i.e. in a region well-probed by CO, tends to produce an undesired “spike” in the CO

line core. Note that by construction, these solutions have significant HCN amounts in the upper atmosphere only down to 750, 550 and 350 km. In the first two cases, this is noticeably shallower than in one case considered before (uniform HCN mixing down to $z_0 = 460$ km and with $q_0 = 4 \times 10^{-5}$, see Fig. 6, blue dotted line); the difference is due to the inclusion, in the present exercise, of the lower atmosphere component, which by preferentially contributing to the satellite lines, modifies the required distribution of HCN opacity in the upper atmosphere.

We conclude that when allowance is made for the presence of low-altitude (<200 km) HCN, the CO and HCN data taken together do not exclude the presence of a warm (92-98 K) upper layer located above ~ 450 km, warm enough that the HCN amounts indicated by the data do not require HCN supersaturation. However we will show below (Section 5.1.1.) that this kind of profile is inconsistent with measurements from New Horizons/Alice.

4.3. $HC^{15}N$ and HC_3N upper limits

As indicated in Section 3, the $HC^{15}N(4-3)$ transition at 344.200 GHz was not detected with a 1σ rms noise level of 1.9 mJy per 0.488 MHz resolution. Using our best fit HCN model (light blue line from Fig. 6) and scaling it by a vertically constant isotopic ratio factor, we determine that the non-detection implies a lower limit of the $HC^{14}N / HC^{15}N$ ratio equal to 125 at 2σ confidence level (Fig. 10). Thus and interestingly, the data readily exclude a Titan-like isotope ratio ($HC^{14}N / HC^{15}N \sim 60$; Vinatier et al., 2007). In contrast, the lower limit of 125 is consistent with the telluric ($^{14}N/^{15}N \sim 270$), cometary ($^{14}N/^{15}N \sim 125-150$) and primordial solar nebula ($^{14}N/^{15}N \sim 440$, as measured in Jupiter, a meteoritic inclusion and the bulk Sun) isotope ratios (for a review see Füri and Marty, 2015).

Translating the result into the bulk $^{14}N/^{15}N$ ratio in Pluto's atmosphere, and ultimately into the $^{14}N/^{15}N$ ratio in the building blocks that formed Pluto, is however a complex problem. On Titan, the high enrichment in $HC^{15}N$ results from the combination of a significant ^{15}N enrichment in the bulk N_2 atmosphere ($^{14}N/^{15}N = 168$, Niemann et al., 2005, 2010) with a photolysis fractionation effect in the HCN formation, i.e. the self-shielding of $^{14}N_2$ from solar UV (Liang et al., 2007). The bulk $^{14}N/^{15}N$ ratio in Titan N_2 was initially interpreted by a large preferential escape of $^{14}N_2$ over the evolution of Titan (Niemann et al., 2005). This scenario was questioned by Mandt et al. (2014), who found that escape does not significantly fractionate Titan's N_2 and concluded that Titan's N_2 isotope ratio was primordial. Their result, however, was in turn questioned by Johnson et al. (2016), who found that the escape rates used in Mandt et al. are not necessarily correct

for fractionation. At any rate, given the very small escape rates at Pluto now evidenced (Gladstone et al., 2016), it may be expected that the $^{14}\text{N}/^{15}\text{N}$ ratio has not significantly fractionated over Pluto’s history. However, isotope fractionation might also occur at sublimation and condensation so that the $^{14}\text{N}/^{15}\text{N}$ in N_2 gas may not necessarily reflect that in Pluto’s ices. Fractionation at sublimation is observed for water $^{18}\text{O}/^{16}\text{O}$ and D/H in terrestrial snow and ice (Sokratov and Golubev, 1999, though fractionation factors are not available) but to our knowledge the process is not documented for N_2 . In any case, the first task would be to model out the photolytic fractionation effect on HCN. On Titan, the differential self-shielding of $^{14}\text{N}_2$ from solar UV leads to a maximum enhancement of the $^{14}\text{N}^{15}\text{N}/^{14}\text{N}_2$ photolysis rate ratio by a factor 25 at 760 km altitude (Liang et al., 2007). The equivalent pressure level (1.5×10^{-8} bar) occurs at ~ 340 km in Pluto’s atmosphere. The HCN observations probe the entire atmosphere from the surface to ~ 900 km, i.e. presumably sample both regions of enhanced $\text{HC}^{15}\text{N} / \text{HC}^{14}\text{N}$ ratio due to photolytic fractionation and regions of “background” ratios. A detailed model would thus be needed for a proper interpretation of our upper limit in terms of the current $^{14}\text{N}/^{15}\text{N}$ in Pluto’s atmosphere.

Similarly, the $\text{HC}_3\text{N}(38-37)$ and $\text{HC}_3\text{N}(39-38)$ transitions at 345.609 and 354.697 GHz are not detected, with 1σ rms of 3.28 mJy per 0.141 MHz resolution for the former and 2.85 mJy per 0.282 MHz resolution for the latter. Converting those into an upper limit of the HC_3N column density requires an assumption on the species’ vertical profile. Assuming here for simplicity that HC_3N has the same distribution as our best fit HCN model (light blue line from Fig. 6), we find an upper limit of 1/10 for the $\text{HC}_3\text{N} / \text{HCN}$ mixing ratio, corresponding to a maximum HC_3N column density of $2 \times 10^{13} \text{ cm}^{-2}$ (Fig. 10). Given the crude assumption of identical vertical distributions for HCN and HC_3N , this upper limit should only be considered as typical, and should be re-derived with realistic photochemically-based vertical profiles for HC_3N when those become available.

5. Discussion

5.1. Thermal profile: comparison with New Horizons/Alice and ground-based stellar occultations measurements

In the preceding, standard temperature profiles from New Horizons (Gladstone et al., 2016) and ground-based occultations (Dias-Oliveira et al., 2015) were only used as a priori guesses when retrieving thermal profiles from CO. Conversely, our solution thermal profiles can be tested against these observa-

tional constraints.

5.1.1. *New Horizons/Alice*

The primary observables relevant to thermal profile are the line-of-sight (LOS) column densities of the major gases (N_2 and CH_4). These are the data that led to the establishment of the standard temperature profile in Gladstone et al. (2016). Using several of the previously discussed thermal profiles, we constructed a diffusion model for the CH_4 - N_2 mixture, using the formalism of Yelle et al. (2006) for two gases in comparable abundance. Free parameters are the surface CH_4 mole fraction q_{0,CH_4} and the vertical eddy diffusion coefficient K_z profile. We also specify an effective CH_4 loss rate of $1.2 \times 10^{26} \text{ s}^{-1}$ at the top of the model, meant to represent the combined effect of the actual CH_4 escape (with rate $\sim 5 \times 10^{25} \text{ s}^{-1}$) and of the CH_4 photolysis – which is not explicitly included in the model. As discussed by Yelle et al. (2008), any other value of the escape rate can be equivalently handled by the use of another K_z profile. Fig. 11 compares the Alice LOS data (as shown in Gladstone et al. (2016), and kindly provided to us by J. Kammer) to models. LOS columns above 850 km for N_2 and 250 km for CH_4 , which are the most reliable, are considered. For the nominal thermal profile (black line), we find that a good fit of the CH_4 and N_2 LOS columns is achieved for $q_{0,\text{CH}_4} = 0.65 \%$ and $K_z = 1 \times 10^6 \text{ cm}^2\text{s}^{-1}$ above 200 km (the exact K_z profile used is shown in the inset of Fig. 10). q_{0,CH_4} is generally consistent with the CH_4 abundance (0.3 - 0.6 %) measured in 2008 and 2012 by (Lellouch et al., 2009, 2015a). The solution parameters are slightly different but rather consistent from those given in the SOM of Gladstone et al. ($q_{0,\text{CH}_4} = 0.60\text{-}0.84 \%$, $K_z = (1.5\text{--}3) \times 10^6 \text{ cm}^2\text{s}^{-1}$). We regard the fit in Fig. 11 as evidence that our nominal thermal profile is consistent with the Alice data. In contrast, the alternate thermal profiles constructed previously to attempt to avoid HCN supersaturation (with a cold mesopause and a warm $\sim 95 \text{ K}$ layer), are clearly at odds with the data, as they would produce an incorrect slope of the CH_4 LOS columns in some part of the atmosphere; additionally, except for the profile in which the warm layer occurs at the highest altitude, these profiles lead to an overestimate of the N_2 LOS columns above 850 km altitude. We conclude that alternate solutions with an HCN profile at saturation, while not excluded from the sole point-of-view of the ALMA data, are not viable, and we dismiss the associated thermal profiles.

5.1.2. Stellar occultations

As outlined previously, thermal profiles retrieved from CO robustly exhibit a 65-70 K temperature at 250-400 km, i.e. somewhat colder than thermal profiles derived from stellar occultations (Dias-Oliveira et al., 2015; Sicardy et al., 2016), which have $T = 81 \pm 6$ K above 200 km. The difference (2σ) is barely significant, as occultation data bear little information on conditions above ~ 250 km. However, our retrieved profiles are also colder than the occultation profiles by 4-10 K over 50-200 km, in which range they also show considerable variability depending on the a priori used (see inset of Fig. 12). We calculated synthetic occultation profiles for a variety of thermal profiles for direct comparison with observed occultation curves; in practice, we used the high S/N 2012 July 18 occultation observed with VLT/NaCO. Note that although our current thermal profile has a surface pressure of 12 μbar , we here rescaled the density profiles using $p_{surf} = 11.6$ μbar , the value minimizing the residuals of our nominal model with respect to observations. Fig. 12 shows the comparison of the observed vs calculated fluxes as a function of distance from Pluto’s shadow center, for the five thermal profiles shown in inset. While, unsurprisingly, the “cold Dias-Oliveira (DO15 + 69 K)” profile matches the occultation data well, none of the other profiles provides a good representation of the data. In particular, the New Horizons standard profile (Gladstone et al., 2016) is markedly inconsistent with the stellar occultation data, as can be best seen from the residuals in the bottom of Fig. 12. Thus, although the published REX profiles from July 14, 2015 (see Fig. 1 of Gladstone et al. (2016)) and the occultation profiles from Dias-Oliveira et al. (2015) both show $T \sim 110$ K at 30-50 km, the mutual consistency between the two datasets will need to be assessed carefully⁶. Thermal profiles retrieved from ALMA CO using either Gladstone et al. (2016) or Dias-Oliveira et al. (2015) as a priori are also at odds with the occultation data. Finally, our nominal profile, while improving the fit compared to the three previous cases, still produces residual “oscillations” (red curves) that indicate an inconsistency with the occultation data. Given these mismatches, the 11.6 μbar adopted in this exercise should not be regarded as a new, improved value of p_{surf} when compared with $p_{surf} = 11.15$ μbar as estimated for mid-2012 by Dias-Oliveira et al. (2015).

⁶Note also that the REX-derived surface pressure are 10 ± 1 and 11 ± 1 μbar , vs 11.9 – 13.7 μbar based on the June 29, 2015 stellar occultation (Sicardy et al., 2016) and these small differences still remain to be reconciled.

Occultations probe near the terminators and at specific latitudes, while our observations are dayside and disk-integrated. However, it is unlikely that thermal profile differences arise from spatial and/or temporal (i.e., 2012 vs 2015) variations. This is because radiative time constants in Pluto’s atmosphere are long (estimated to be in the range 10–15 yr by Strobel et al., 1996), leading to small longitudinal and equator-to-pole temperature differences. Both Toigo et al. (2015) and Forget et al. (2016) estimate that meridional variations in temperature are less than 1 K for the New Horizons epoch, though, interestingly, Toigo et al. (their Fig. 16) find that the pole-to-Equator gradient in the middle atmosphere could have reached ~ 10 K in the last few decades. We note however that the eight temperature profiles inverted from four lightcurves in 2012 and 2013 by Dias-Oliveira et al. (2015) show variability at the ± 5 K level in the first ~ 200 km (although in no case is the stratopause colder than 109 K), which would not be expected in view of the above considerations, and if real might point to dynamical effects.

As discussed in Section 4.1.2 and Fig. 2, the colder temperatures over 50–200 km are required for an optimum fit of the CO line core, so the inconsistency with the stellar occultation curves does not seem obvious to resolve. Admittedly, the “cold Dias-Oliveira” profile with upper atmosphere at 69 K would provide a better overall compromise when fitting together the CO line and the VLT/NaCO occultation curve. However, the discrepancies outlined in Fig. 12 rather suggest that a global fit of all the constraints relevant to Pluto’s thermal structure (i.e., stellar occultations, REX, Alice solar occultation, CH₄ near-IR and ALMA CO spectroscopy) should eventually be performed. For now, while the well-marked mesosphere and the $T = 70 \pm 2$ K temperature at 300 km are well defined from our retrievals, the lower mesosphere and stratopause temperatures must be considered as more uncertain. As discussed above, this does not impact our conclusions on the HCN distribution, but makes the interpretation of the HCN amounts in the lower atmosphere more ambiguous.

5.2. CO abundance

We determine a CO mole fraction of 515 ± 40 ppm for a surface pressure $p_{surf} = 12 \mu\text{bar}$, rescaling as $(12 \mu\text{bar}/p_{surf})^{1.9}$ for other values of p_{surf} . The associated surface-referred column density is 0.100 ± 0.008 cm-am for $p_{surf} = 12 \mu\text{bar}$, and scales as $(12 \mu\text{bar}/p_{surf})^{0.9}$. These figures are much more accurate than, yet nicely consistent with, results from Pluto’s $2.3 \mu\text{m}$ spectrum (Lellouch et al., 2011). Specifically, these authors inferred q_{CO}

$= 500_{-250}^{+1000}$ ppm, where most of the uncertainty was due to signal-to-noise limitations (and to a much lower extent to the uncertain lower atmosphere thermal structure and surface pressure at that time). Based on Table 1 from Lellouch et al. (2011), for $p_{surf} = 12 \mu\text{bar}$, the best fit CO mole fraction and column density from the $2.3 \mu\text{m}$ data would have been 530 ppm and 0.09 cm-am, respectively, but still with a factor ~ 2 uncertainty. Our new determination thus validates the “strong evidence ($6\text{-}\sigma$)” for gaseous CO reported by Lellouch et al. (2011) as being indeed a detection, while superseding it by far in accuracy. In contrast, the formal $4.5\text{-}\sigma$ detection of the CO(2-1) line by Bockelée-Morvan et al. (2001), that was modelled in terms of a much higher 1.2 % - 7 % CO mixing ratio, must indeed have been affected by galactic contamination, and as mentioned previously, was cautiously considered as such by the authors.

Attempts to interpret the CO atmospheric abundance in terms of surface-atmosphere interactions were presented by Lellouch et al. (2011). Here the key parameter is the CO/N₂ mixing ratio in the surface ice. With the ~ 0.5 % CO/N₂ value originally inferred by Owen et al. (1993), an atmospheric abundance of ~ 500 ppm (0.05%) is consistent with an ideal solid solution in equilibrium with the atmosphere (i.e., Raoult’s law). Lellouch et al. (2011) noted that this interpretation falls apart if updated CO/N₂ ice ratios of 0.08-0.2 % (Douté et al., 1999) were used. Instead, they proposed that the consistency, within error bars, of these latter values with their 0.025-0.15 % CO gas mixing ratios favored the so-called “detailed balancing model” proposed by Trafton et al. (1997). An alternative explanation in terms of pure CO ice patches enriching the atmosphere in CO gas was also mentioned but rejected on thermodynamical grounds. A recent analysis of new near-IR spectra (Merlin, 2015) now suggests (disk-averaged) CO/N₂ ice ratios of 2500-5000 ppm, *not* consistent with our updated atmospheric mixing ratio of 515 ppm, challenging the detailed balancing explanation and favoring again the ideal solution interpretation. Even more recently, a post-New Horizons global climate model (GCM) for Pluto has been developed (Forget et al., 2016). In this model, which includes the N₂, CH₄ and CO cycles, volatiles sublimate according to Raoult’s law and their surface abundances. Regarding CO, model findings are that CO, which is almost as volatile as N₂, only condenses when N₂ ice is present at the surface, and never forms separate CO deposits. This is in agreement with the strongly localized distribution of CO ice in to Sputnik Planum (Grundy et al., 2016), where N₂ ice also appears concentrated (but not restricted to). In the GCM, the CO cycle is dominated by a condensation-sublimation cycle inside Sputnik Planum. Interestingly, the model, which uses a CO/N₂ ice ratio of 0.3 % from Merlin

(2015), predicts an atmospheric CO/N₂ of 0.03 %. Although this is not yet fully consistent with our value, it suggests that the essential physics is captured. Model predictions should be improved by using the CO ice mixing ratio in Sputnik Planum when the latter becomes available from New Horizons.

5.3. HCN profile, supersaturation and photochemical models

HCN column densities associated with our various line fits and retrievals span the range $(1.2\text{--}2.0)\times 10^{14}$ cm⁻². Although the precise vertical distribution cannot be unambiguously determined from lines of moderate optical thickness, the data support a bimodal HCN distribution, with a high-altitude (>500 km) component with highly supersaturated $(1.5\text{--}5)\times 10^{-5}$ mole fraction, and a near-stratopause component at $10^{-7}\text{--}10^{-8}$. In the best fit empirical model, the upper (resp. lower) atmosphere components have 5×10^{13} (resp. 1.5×10^{14}) cm⁻² columns.

HCN is the prime nitrile to be expected in a N₂-CH₄ atmosphere and had been predicted for Pluto (Lara et al., 1997; Summers et al., 1997; Krasnopolsky and Cruikshank, 1999; Gladstone et al., 2015). Altogether, these models have envisaged a vast range of HCN mixing ratios and distributions, and it is a little difficult to track down the reasons for the differences, although some must result from different temperature profile assumptions. Nonetheless, almost all of these models appear to have severely overpredicted the amounts of HCN in Pluto’s atmosphere. For example, the HCN column density in Krasnopolsky and Cruikshank is quoted as 6×10^{16} cm⁻², a factor of 400 too large, and the HCN mixing ratio in the upper atmosphere, $\sim 1\times 10^{-3}$, is 20–60 times too large. (Note also that their calculated HC₃N column was 3.4×10^{16} cm⁻², more than three orders of magnitude larger than our upper limit). Similarly, in the pre-New Horizons models by (Gladstone et al., 2015), most of the HCN profiles have a $(3\text{--}5)\times 10^{-4}$ upper atmosphere mixing ratio. Lara et al. (1997), who used a thermal profile with a marked temperature decrease above the stratopause (from Strobel et al. 1996) predicted a pile-up of HCN over 30–200 km with a typical $\sim 3\times 10^8$ cm⁻³ number density in this range, a consequence of atmospheric condensation. Still, their HCN column was about 5×10^{15} cm⁻², a factor 30 too large. Summers et al. (1997) also predicted HCN restricted to the lower atmosphere, with $\sim 10^7$ cm⁻³ over 50–150 km, implying a $\sim 10^{14}$ cm⁻² column density, in rather good agreement with our measurement, but missing the upper atmosphere component.

Once produced in the upper atmosphere, HCN must be transported downwards to a condensation sink, and be further transported in solid

form down to the warmer stratopause region where in principle it can re-evaporate. An order-of-magnitude estimate of the HCN production rate can be obtained by equating the chemical column net production rate P to the downward flux, i.e. $P = a_{HCN} / \tau$, where the time constant τ is equal to $2H^2 / \max(K_z, D_{HCN-N_2})$. Here, a_{HCN} is the upper atmosphere component column density, H is the atmospheric scale height, and K_z and D_{HCN-N_2} are the eddy and molecular diffusion coefficients, respectively. Using $a_{HCN} = 5 \times 10^{13} \text{ cm}^{-2}$, $H = 65 \text{ km}$, $K_z = 10^6 \text{ cm}^2\text{s}^{-1}$ and $D_{HCN-N_2} = 1.5 \times 10^7 \text{ cm}^2\text{s}^{-1}$ at 450 km, leads to a column net production rate $P = 0.9 \times 10^7 \text{ cm}^{-2}\text{s}^{-1}$ at this altitude, i.e. $P = 1.7 \times 10^7 \text{ cm}^{-2}\text{s}^{-1}$ referred to the surface. This estimate should be compared to predictions based on photochemical models.

The most remarkable of our findings is the fact that Pluto's upper atmosphere, albeit at $\sim 70 \text{ K}$, contains large HCN amounts, implying a huge supersaturation with respect to local conditions (e.g. 7-8 orders of magnitude at 800 km). Supersaturation of condensible species is known to occur in other planetary atmospheres. In the Earth's upper troposphere, enhancements of H_2O gas over the gas-ice equilibrium are being frequently observed, with relative humidity levels routinely of 120-150 % and (rarely) up to $\sim 250 \%$ (Gettelman et al., 2006). In the Martian atmosphere, supersaturation of water vapor is clearly observed, with saturation ratios up to 5-10 over 30-50 km altitude (Maltagliati et al., 2011), and large supersaturation of CO_2 in the upper atmosphere is indicated by the occasional existence of temperatures significantly below the CO_2 frost point over 90-120 km (Forget et al., 2009). Supersaturation is commonly assumed to result from the lack of condensation nuclei in clear atmospheres (or parts thereof), restricting the role of heterogeneous nucleation and possibly leaving homogeneous nucleation as the only mechanism for limiting the amount of condensibles in the gas phase. Nonetheless, supersaturation ratios by orders of magnitude have not been observed before in a planetary atmosphere.

Although's Pluto's atmosphere is haze-rich, the haze in New Horizons images is detected up to $\sim 200 \text{ km}$ only, with a brightness scale height of 30 km over 100-200 km, and an estimated concentration of $0.8 \text{ particle cm}^{-3}$ at the surface (Stern et al., 2015; Gladstone et al., 2016). Assuming that the haze is well mixed with gas, the haze concentration would be $\sim 10^{-6} \text{ particle cm}^{-3}$ at 800 km, where the pressure is about $2 \times 10^{-11} \text{ bar}$. These extremely small numbers may explain the strong inefficiency of neutral homogeneous and heterogeneous nucleations in Pluto's upper atmosphere.

Development of a coupled photochemical-microphysical-ionospheric model for Pluto is in progress (Lavvas et al., in prep.). The model is based on the

Gladstone et al. (2016) standard temperature profile. Regarding condensation, as for now, the model includes homogeneous neutral nucleation as well as nucleation of HCN due to the presence of ions in Pluto’s upper atmosphere (whose abundance is calculated self-consistently). A preliminary HCN profile resulting from the coupled model is shown in Fig. 7. Testing it against the ALMA observations indicates that a good agreement is obtained by uniformly dividing the calculated HCN mixing ratio in the model by 2. This rescaled profile has a HCN mole fraction of 4×10^{-5} at 800 km and a column density of $1.6 \times 10^{14} \text{ cm}^{-2}$, in full agreement with previous inferences from manual fitting and line inversion. Although the physical model must still be fine-tuned and its sensitivity to thermal profile assumptions studied, this agreement is encouraging and demonstrates that a huge degree of supersaturation is a realistic situation in Pluto’s upper atmosphere. In the lower atmosphere, where haze condensation nuclei are available and where the kinetics of the condensation process are more efficient, HCN tends to follow local saturation. Due to the temperature increase towards the stratopause, the evaporation of ice particles re-enriches the atmosphere in HCN gas. In this respect, an important observational constraint is that the HCN amount in the lower atmosphere is consistent with saturation at 106 K, which is also the preferred stratopause temperature in our retrievals based on CO. If the stratopause is actually warmer (e.g. at 110 K, as suggested by stellar occultation and REX data), then HCN must be *undersaturated* in this region (by up to a factor ~ 10 , exceeding the uncertainty on the vapor pressure expression from Fray and Schmitt, 2009). To account for this putative situation, Lavvas et al. (in prep.) propose that ice particles could be big enough to fall through the region of the temperature maximum faster than they can evaporate, or more likely that the abundance of HCN (and several hydrocarbons) may be reduced by heterogeneous processes taking place at the surface of the haze particles and that inhibit their evaporation.

The above suggests that HCN condensates are significant contributors to Pluto’s haze. In addition, the ultimate sedimentation of the haze particles should lead to the presence of HCN ice on the surface, although its detectability is uncertain due to the fact that seasonal exchanges of N_2 (typically 10 g cm^{-2} per Pluto year, e.g. Olkin et al., 2015) and other volatiles (CH_4 , CO) occur at a much faster rate, presumably burying HCN ice under layers of more volatile species. We still note that a tentative detection of HCN ice has been reported on Triton (Burgdorf et al., 2010), but so far was not confirmed.

5.4. Implications for heating budget

Even prior to their detection, CO and HCN have been identified as possible important species for Pluto’s atmosphere heating budget. Lellouch (1994) initially suggested that in addition to the heating/cooling “thermostat” role of CH₄ first identified by Yelle & Lunine (1989), cooling due to LTE emission from CO rotational lines should be significant, given the then estimated abundance of CO (10^{-4} – 10^{-3}). Using a much more extensive radiative-convective model, Strobel et al. (1996) first suggested the possibility of a mild negative temperature gradient (-0.0 – 0.1 K/ km) in the 1–2 μ bar pressure range. These models were updated by Zalucha et al. (2011a,b) and Zhu et al. (2014) to include new observational constraints on Pluto’s atmosphere composition (CH₄ = 5×10^{-3} , CO = 5×10^{-4}) and near-surface structure (Lellouch et al., 2009, 2011). Nonetheless, these updated models confirmed the essential features of the earlier Strobel et al. (1996) models, continuing to show only weak negative temperature gradients above the stratopause, typically a ~ 5 K decrease over a 300 km range for a CO mixing ratio of 5×10^{-4} .

The existence and origin of a well-marked mesosphere with an upper atmosphere at ~ 80 K was first discussed in Dias-Oliveira et al. (2015), although a similar behaviour had in fact been observed in several earlier stellar occultation profiles. Noting that the above N₂-CH₄-CO models were unable to explain the ~ 30 K decrease they observed over 30–180 km (i.e. a -0.2 K/km gradient) unless CO was about 40 times larger than observed (i.e. 200×10^{-4}), these authors considered HCN cooling, by analogy with Titan’s thermosphere, where radiation in the intense rotational lines of HCN equilibrates the solar UV heating rate (Yelle, 1991). Although Dias-Oliveira et al. (2015) did not design a complete radiative model, they estimated the amount of HCN needed to compete with rotational cooling due to a 200×10^{-4} CO mole fraction. They concluded that a uniform HCN profile at $\sim 5 \times 10^{-5}$ was required to explain their temperature profile, implying a strong supersaturation of HCN *throughout* the atmosphere.

With an upper atmosphere at ~ 70 K, temperature profiles deduced from New Horizons/Alice and from CO in the present study confirm and exacerbate the magnitude of the mesospheric temperature decrease. Constraints on HCN we infer in this study indicate that HCN cooling cannot be the sole cause for this gradient. Remarkably enough, the well determined HCN mole fraction of 4×10^{-5} at 800 km compares well to the estimate from Dias-Oliveira et al. (2015), but their estimate was based on a 80 K upper atmosphere temperature, vs 70 K as now established. Furthermore, the HCN data strongly exclude that HCN is well mixed down to the surface and thus

cannot make up for the entire required cooling. The New Horizons/Alice hydrocarbon detections (Gladstone et al., 2016) indicate that C_2H_2 non-LTE vibrational cooling in its ν_5 band at $13.7 \mu\text{m}$ may be important near the warm stratopause at 30 km. However, detailed calculations to be published elsewhere (Strobel et al. in prep.) indicate that C_2H_2 cooling falls off rapidly with increasing altitude, in conjunction with the pressure decrease that causes this emission to become more non-LTE and the temperature decrease that shifts this emission even further away from the Planck function maximum. Specifically, these calculations find that the C_2H_2 cooling rate falls below that of CO below ~ 230 km. At this altitude and up to ~ 500 km, both our HCN line inversions and the physical model from Lavvas et al. (in prep.) matching the ALMA data (i.e. rescaled by 1/2) indicate HCN mole fractions lower than 2×10^{-5} , i.e. unable to produce enough cooling. Therefore, in addition to the HCN deficit in the upper atmosphere to explain a ~ 70 K atmosphere, the most critical problem is the lack of an identified cooling species in the 230-500 km region. To illustrate the magnitude of the problem, Fig. 13 shows calculated temperature profiles including cooling by CO, C_2H_2 (as constrained by the New Horizons solar occultation data) and HCN, using several HCN profiles, along with observational temperature profiles. The comparison of model temperatures for the rescaled Lavvas et al. profile (dark blue) with a case with no HCN (light blue) demonstrates that HCN is a relatively minor cooling agent in Pluto’s atmosphere, causing a mere reduction of the atmospheric temperatures by 5-10 K at most above 400 km, and unable to explain temperatures below 80 K. Reaching the asymptotic 70 K temperature would require an HCN profile (red) more similar to the pre-New Horizons model of Gladstone et al. (2015), in excess of the observed profile by a factor 20-200. Even in this case, the calculated temperatures over 100-300 km exceed those inferred from New Horizons and from the present study, pointing to too small cooling rates.

Thus, Pluto’s atmosphere heating budget remains poorly understood. It appears that another radiatively active constituent (perhaps haze, or another as yet undetected gas) or non-radiative effects are required, but identifying those does not seem straightforward. In particular, any haze cooling should be restricted to levels (< 300 km) where haze is apparent in New Horizons images, and the presence of haze above ~ 450 km would contradict the observed HCN supersaturation there.

6. Summary

Based on high signal-to-noise ALMA observations performed in June 2015, we report the first observation of CO in Pluto’s atmosphere at sub-millimeter wavelengths, and the first detection of HCN. Based on radiative transfer fits including optimal inversion techniques, we find that the CO and HCN lines probe Pluto’s atmosphere up to ~ 450 km and ~ 900 km altitude, respectively, with a large contribution due to limb emission. We reach the following conclusions:

- The CO mole fraction in Pluto’s atmosphere is 515 ± 40 ppm for a $12 \mu\text{bar}$ surface pressure. While this essentially confirms the amounts previously estimated from near-IR spectroscopy, the much higher accuracy demonstrates that the gas CO mole fraction is significantly lower than the CO:N₂ ratio in the ice phase. This, along with recent climate model results including the N₂, CH₄ and CO cycles, favors the scenario of an ideal N₂:CO solid solution feeding both gases into the atmosphere, and more complex interpretations such as the detailed-balancing model do not seem supported any longer.
- The CO line profile gives clear evidence for a well-marked temperature decrease over ~ 50 -400 km altitude, with a best-determined temperature of 70 ± 2 K at 300 km, somewhat lower than those previously estimated from stellar occultations (81 ± 6 K), and in agreement with recent inferences from New Horizons / Alice solar occultation data. The preferred temperature profiles deduced from CO have a ~ 106 K stratopause temperature, also colder than that deduced from stellar occultation profiles (~ 110 K). A global fit of all relevant datasets should be eventually performed, with the goal of defining the “best” thermal profile for Pluto’s atmosphere.
- With an HCN mole fraction $> 1.5 \times 10^{-5}$ above 450 km and a best determined value of 4×10^{-5} near 800 km, Pluto’s upper atmosphere is particularly HCN-rich. Although technically this could be the sign of a warm (> 92 K) upper atmosphere layer, still consistent with constraints from CO, this situation would violate the Alice CH₄ and N₂ measurements. Instead, the HCN mixing ratios imply a supersaturation of HCN in the upper atmosphere to a degree (7-8 orders of magnitude) hitherto unseen in planetary atmospheres, and probably related to the lack of condensation nuclei above the haze region. Optimum fit of the HCN line indicates that HCN is also present in the

bottom ~ 100 km of the atmosphere, with a 10^{-8} - 10^{-7} mole fraction which, depending on the precise stratopause temperature, could be at saturation or undersaturated by up to a factor ~ 10 .

- The HCN column is $(1.6 \pm 0.4) \times 10^{14} \text{ cm}^{-2}$, including $\sim 5 \times 10^{13} \text{ cm}^{-2}$ in the upper atmosphere (> 450 km). This suggests a surface-referred net column production rate of $\sim 2 \times 10^7 \text{ cm}^{-2} \text{ s}^{-1}$.
- Although HCN has been previously identified as a potential cooling agent in Pluto's atmosphere, the HCN amounts determined in this study appear insufficient to explain the well-marked mesosphere and upper atmosphere temperature, so that the heat balance of Pluto's middle and atmosphere remains to be understood.
- From the non-detection of HC_3N and HC^{15}N lines, we infer upper limits to the HC_3N column density ($< 2 \times 10^{13} \text{ cm}^{-2}$) and to the HC^{15}N / HC^{14}N isotopic ratio ($< 1/125$).

Given the strengths of the CO and HCN signals measured by ALMA, it will be possible, in the future, to obtain moderately spatially-resolved maps of their emission. Specific goals would include (i) the characterization of the thermal field over 50-400 km (ii) the search for horizontal variations of the HCN content or of temperature in the upper atmosphere (> 500 km) (iii) constraints on the upper atmosphere dynamics from (more challenging) direct wind measurements. The great sensitivity of ALMA also makes additional molecular searches promising. In the mid- and long-term, and along with other Earth-based facilities, ALMA will remain an indispensable asset to monitor the evolution of Pluto's atmosphere composition and thermal state as Pluto recedes from the Sun.

Acknowledgements:

This paper is based on ALMA program 2013.1.00446.S. ALMA is a partnership of ESO (representing its member states), NSF (USA) and NINS (Japan), together with NRC (Canada), NSC and ASIAA (Taiwan), and KASI (Republic of Korea), in cooperation with the Republic of Chile. The Joint ALMA Observatory is operated by ESO, AUI/NRAO and NAOJ. The National Radio Astronomy Observatory is a facility of the National Science

Foundation operated under cooperative agreement by Associated Universities, Inc. Part of the research leading to these results has received funding from the European Research Council under the European Community's H2020 (2014-2020/ERC Grant Agreement 669416 "LUCKY STAR"). We acknowledge useful discussions with N. Fray and B. Schmitt.

References

- Barnes, P.J., 1993. A search for CO emission from the Pluto-Charon system. *Astron. J.* 106, 2540-2543.
- Bockelée-Morvan, D., Lellouch, E., Biver, N., et al., 2001. Search for CO gas in Pluto, Centaurs and Kuiper Belt objects at radio wavelengths. *Astron. Astrophys.* 377, 343-353.
- Buie, M.W., Tholen, D.J., Wasserman, L.H., 1997. Separate lightcurves of Pluto and Charon, *Icarus* 125, 233-244.
- Burgdorf, M., Cruikshank, D.P., Dalle Ore, C.M., et al., 2010. A tentative identification of HCN ice on Triton. *Astrophys. J.* 718, L53-L57.
- Butler, B.J., 2012. Flux density models for Solar System bodies in CASA. ALMA Memo 594, November 2012.
- Butler, B., Gurwell, M., Lellouch, E., et al., 2015. Long wavelength observations of thermal emission from Pluto and Charon with ALMA. 47, id.210.04.
- Conrath, B.J., Gierasch, P.J., Ustinov, E.A., 1998. Thermal structure and para hydrogen fraction on the outer planets from Voyager IRIS measurements. *Icarus* 135, 501517.
- Cornwell, T., Fomalont, E.B., 1999. Self-calibration. In G. B. Taylor, C. L. Carilli, and R. A. Perley, editors, *Synthesis Imaging in Radio Astronomy II*, *Astr. Soc. Pacific Conf. Series*, 180, 187-199.
- Cordiner, M.A., Palmer, M.Y., Nixon, C.A., et al., 2015a. Ethyl cyanide on Titan: spectroscopic detection and mapping using ALMA. *Astrophys. J.* 800, article id. L14, 7 pp.
- Cordiner, M.A., Palmer, M.Y., Nixon, C.A., et al., 2015b. ALMA spectroscopy of Titan's atmosphere: first detections of vinyl cyanide and acetonitrile isotopologues. *Bull. Amer. Astron. Soc.* 47, id.205.03.
- Dias-Oliveira, A., Sicardy, B., Lellouch, E., et al., 2015. Pluto's atmosphere from stellar occultations in 2012 and 2013. *Astrophys. J.* 811, article id. 53, 20 pp.
- Dumouchel, F., Faure, A., Lique, F., 2010. The rotational excitation of HCN and HNC by He: temperature dependence of the collisional rate coefficients. *MNRAS* 406, 2488-2492.

- Douté, S., Schmitt, B., Quirico, E., Owen, T.C., Cruikshank, D.P., de Bergh, C., Geballe, T.R., Roush, T.L., 1999. Evidence for methane segregation at the surface of Pluto. *Icarus* 142, 421-444.
- Elliot, J.L., Ates, A., Babcock, B.A., et al., 2003. The recent expansion of Pluto's atmosphere. *Nature* 424, 165-168.
- Forget, F., Montmessin, F., Bertaux, J.-L., et al., 2009. Density and temperatures of the upper Martian atmosphere measured by stellar occultations with Mars Express SPICAM. *J. Geophys. Res.* 114, E1, CiteID E01004.
- Forget, F., Bertrand, T., Vangvitchith, M., et al., 2016. A post-New Horizons global climate model of Pluto including the N₂, CH₄ and CO cycles. *Icarus*, submitted.
- Fouchet, T., Greathouse, T., Spiga, A., Fletcher, L., Guerlet, S., 2016. Stratospheric aftermath of the 2010 storm on Saturn as observed by the TEXES instrument. I. Temperature structure. *Icarus*, in press.
- Fray, N., and Schmitt, B., 2009. Sublimation of ices of astrophysical interest: A bibliographic review. *Planet. Space Sci.* 57, 2053-2080.
- Füri, E., Marty, B., 2015. Nitrogen isotope variations in the Solar System. *Nature Geoscience*, 8, 515-522.
- Gettelman, A., Fetzer, E.J., Eldering, A., Irion, F.W., 2006. The global distribution of supersaturation in the upper troposphere from the Atmospheric Infrared Sounder. *J. Climate* 19, 6089-6103.
- Gladstone, G.R., Stern, S.A., Ennico, K., et al., 2016. The atmosphere of Pluto as observed by New Horizons. *Science* 351, aad8866.
- Greaves, J.S., Helling, C., Friberg, P., 2011. Discovery of carbon monoxide in the upper atmosphere of Pluto. *MNRAS* 414, L36-L40.
- Gladstone, G.R.; Yung, Y.L., Wong, M.L. 2015, Pluto atmosphere photochemical models for New Horizons, 46th LPSC Conference, 46.3008G.
- Grundy, W.M., Olkin, C.B., Young, L.A., Buie, M.W., Young, E.F., 2013. Near-infrared spectral monitoring of Pluto's ices: Spatial distribution and secular evolution. *Icarus* 223, 710-721.
- Grundy, W.M., Binzel, R.P., Buratti, B.J., et al., 2016. Surface compositions across Pluto and Charon. *Science* 351, aad9189.

- Gurwell, M.A., Butler, B.J., Moullet, A., 2014. Atmospheric CO on Pluto: limits from millimeter-wave spectroscopy. *Bull. Amer. Astron. Soc.* 46, id.401.05.
- Gurwell, M., Lellouch, E., Butler, B., et al., 2015. Detection of atmospheric CO on Pluto with ALMA. *Bull. Amer. Astron. Soc.* 47, id.105.06.
- Hansen, C.J., Paige, D.A., Young, L.A., 2015. Pluto's climate modeled with new observational constraints. *Icarus* 246, 183-191.
- Johnson, R.E., Tucker, O.J., Volkov, A.N., 2016. Evolution of an early Titan atmosphere. *Icarus*, 271, 202-206.
- Koshelev, M.A., Markov, V.N., 2009. Broadening of the J=3-2 spectral line of carbon monoxide by pressure of CO, N₂ and O₂. *J. Quant. Spectrosc. Radiat. Transf.* 110, 526-527.
- Krasnopolsky, V.A, Cruikshank, D.P., 1999. Photochemistry of Pluto's atmosphere and ionosphere near perihelion. *J. Geophys. Res.* 104, E9, 21979-21996.
- van Langevelde, H.J., and Cotton, W.D, 1990. Visibility-based continuum subtraction in spectral line observations with radio synthesis telescopes. *Astron. Astrophys.* 239, L5L8.
- Lara, L.M., Ip, W.-H., Rodrigo, R., 1997. Photochemical models of Pluto's atmosphere. *Icarus* 130, 16-35.
- Lellouch, E., 1994. The thermal structure of Pluto's atmosphere: clear vs hazy models. *Icarus* 108, 255-264.
- Lellouch, E., et al., 2009. Pluto's lower atmosphere structure and methane abundance from high-resolution spectroscopy and stellar occultations. *Astron. Astrophys.* 495, L17-L21.
- Lellouch, E., de Bergh, C., Sicardy, B., Käuffl, H.U., Smette, A., 2011. High resolution spectroscopy of Pluto's atmosphere: detection of the 2.3 μm CH₄ bands and evidence for carbon monoxide. *Astron. Astrophys.* 530, L4.
- Lellouch, E., de Bergh, C., Sicardy, B., et al., 2015a, Exploring the spatial, temporal, and vertical distribution of methane in Pluto's atmosphere. *Icarus* 246, 268-278.

- Lellouch, E., Gurwell, M., Butler, B. et al., 2015b. (134340) Pluto. IAUC 9273.
- Lellouch, E., Gurwell, M., Butler, B. et al., 2015c. Detection of HCN in Pluto's atmosphere. *Bull. Amer. Astron. Soc.* 47, id.105.07.
- Liang, M.-C., Heays, A.N., Lewis, B.R., Gibson, S.T., Yung, Y.L., 2007. Source of nitrogen isotope anomaly in HCN in the atmosphere of Titan. *Astrophys. J.* 664, L115-L118.
- Maltagliati, L., Montmessin, F., Fedorova, A., Korablev, O., Forget, F., Bertaux, J.-L., 2011, Evidence of water vapor in excess of saturation in the atmosphere of Mars. *Science* 333, 1868-1871.
- Mandt, K., Mousis, O., Lunine, J., Gautier, D., 2014. Protosolar ammonia as the unique source of Titan's nitrogen. *Astrophys. J.* 788, id. L24, 5 pp.
- Merlin, F., 2015. New constraints on the surface of Pluto. *Astron. Astrophys.* 582, id.A39, 9 pp.
- Muders, D., Wyrowski, F., Lightfoot, J., et al., 2014. The ALMA Pipeline. In N. Manset and P. Forshay, editors, *Astronomical Data Analysis Software and Systems XXIII*, May 2014. , 2014. The ALMA Pipeline. In N. Manset and P. Forshay, editors, *Astronomical Data Analysis Software and Systems XXIII*, May 2014.
- Müller, H.S.P., Thorwirth, S., Roth, D.A., Winnewisser, G., 2011. The Cologne Database for Molecular Spectroscopy, CDMS. *Astron. Astrophys.*, 370, L49-L52.
- Niemann, H.B., Atreya, S.K., Bauer, S.J., et al., 2005. The abundances of constituents of Titan's atmosphere from the GCMS instrument on the Huygens probe. *Nature* 438, 779-784.
- Niemann, H.B., Atreya, S.K., Demick, J.E., et al., 2010. Composition of Titans lower atmosphere and simple surface volatiles as measured by the CassiniHuygens probe gas chromatograph mass spectrometer experiment. *J. Geophys. Res.*, 115, E12006, doi:10.1029/2010JE003659.
- Olkin, C.B., Young, L.A., Borncamp, D., et al., 2015. Evidence that Pluto's atmosphere does not collapse from occultations including the 2013 May 04 event. *Icarus* 246, 220-225.

- Owen, T.C., Roush, T.L., Cruikshank, D.P., et al., 1993. Surface ices and atmospheric composition of Pluto. *Science* 261, 745-748.
- Priem, D., Rohart, F., Colmont, J.-M., Wlodarczak, G., Bouanich, J.-P., 2000. Lineshape study of the J=3-2 rotational transition of CO perturbed by N₂ and O₂. *J. Mol. Spectro.* 517, 435-454.
- Rezac, L., Kutepov, A.A., Faure, A., Hartogh, P., Feofilov, A.G., 2013. Rotational non-LTE in HCN in the thermosphere of Titan: implications for the radiative cooling. *Astron. Astrophys.* 555, A122.
- Rodgers, C.D., et al., 2000. Inverse methods for atmospheric sounding: theory and practice. Vol. 2. World Scientific, Singapore.
- Schmitt, B., et al., 2016. Physical state and distribution of materials at the surface of Pluto from New Horizons LEISA imaging spectrometer. Submitted for publication.
- Sicardy, B., Widemann, T., Lellouch, E., et al., 2003. Large changes in Pluto's atmosphere as revealed by recent stellar occultations. *Nature* 424, 168-170.
- Sicardy, B., Talbot, J., Meza, E., et al., 2016. Pluto's atmosphere from the 2015 June 29 ground-based stellar occultation at the time of the New Horizons flyby. *Ap. J.* 819, L38.
- Sokratov, S.A., and Golubev, V.N., 1999. Snow isotopic content change by sublimation. *J. Glaciology*, 55, 823-828.
- Stern, S.A., Bagenal, F., Ennico, K., et al., 2015. The Pluto system: Initial results from its exploration by New Horizons. *Science* 350, aad1815.
- Strobel, D.F., Zhu, X., Summers, M.E., Stevens, M.H., 1996. On the vertical thermal structure of Pluto's atmosphere. *Icarus* 120, 266-289.
- Summers, M.E., Strobel, D.F., Gladstone, G.R., 1997. Chemical models of Pluto's atmosphere In: Stern, S.A., Tholen, D.J. (Ed.), *Pluto and Charon*, p. 391.
- Thompson, A.R., Moran, J.M., and Swenson, G.W., 2001. *Interferometry and Synthesis in Radio Astronomy*, 2nd Edition. Wiley-Interscience, New York, New York.

- Toigo, A.D., French, R.G., Gierasch, P.J., et al., 2015. General circulation models of the dynamics of Pluto's volatile transport on the eve of the New Horizons encounter *Icarus* 254, 306-323.
- Trafton, L.M., Hunten, D.M., Zahnle, K.J., McNutt Jr., R.L., 1997. Escape processes at Pluto and Charon. In: Stern, S.A., Tholen, D.J. (Eds.), *Pluto and Charon*. Univ. of Arizona Press, Tucson, pp. 475-522.
- Vinatier, S., Bézard, B., Fouchet, T., et al., 2007. Vertical abundance profiles of hydrocarbons in Titan's atmosphere at 15°S and 80°N retrieved from Cassini/CIRS spectra. *Icarus* 188, 120-138.
- Yang, C., Buldyreva, J., Gordon, I.E., et al., 2008. Oxygen, nitrogen and air broadening of HCN spectral lines at terahertz frequencies. *J. Quant. Spectrosc. Radiat. Transf.* 109, 2857-2868.
- Yelle, R.V., 1991. Non-LTE models of Titan's upper atmosphere. *Astrophys. J.* 383, 380-400.
- Yelle, R.V., Borggren, N., de la Haye, V., et al., 2006. The vertical structure of Titan's upper atmosphere from Cassini Ion Neutral Mass Spectrometer measurements, *Icarus* 182, 567-576.
- Yelle, R.V., Cui, J., Müller-Wodarg, I.C.F., 2008. Methane escape from Titan's atmosphere. *J. Geophys. Res.* 113, E10, CiteID E10003.
- Yelle, R.V., Lunine, J.I., 1989. Evidence for a molecule heavier than methane in the atmosphere of Pluto. *Nature* 339, 288-290.
- Young, L.A., 2013. Pluto's seasons: new predictions for New Horizons. *Ap. J. Lett.* 766, L22 (6pp).
- Zalucha, A., Gulbis, A.A.S., Zhu, X., Strobel, D.F., Elliot, J.L., 2011a. An analysis of Pluto occultation light curves using an atmospheric radiative-conductive model. *Icarus* 211, 804-818.
- Zalucha, X., Zhu, A.M., Gulbis, A.A.S., Strobel, D.F., Elliot, J.L., 2011b. An investigation of Pluto's troposphere using stellar occultation light curves and an atmospheric radiative-conductive-convective model. *Icarus* 214, 685-700.
- Zhu, X., Strobel, D.F. and Erwin, J.T. 2014. The density and thermal structure of Pluto's atmosphere and associated escape processes and rates. *Icarus* 228, 301-314.

- Young, L.A., Elliot, J.L., Tokunaga, A., de Bergh, C., Owen, T., 1997. Detection of gaseous methane on Pluto. *Icarus* 127, 258-262.
- Young, L. A., Cook, J.C., Yelle, R. V., Young, E. F., 2001. Upper limits on gaseous CO at Pluto and Triton from high-resolution near-IR spectroscopy. *Icarus* 153, 148-156.
- Zangari, A., 2015. A meta-analysis of coordinate systems and bibliography of their use on Pluto from Charon's discovery to the present day. *Icarus* 246, 93-145.

Figure captions

Fig. 1. Overview of CO(3-2) (top) and HCN(4-3) (bottom) line observations on the two observing days. For HCN, the hyperfine structure is detected on both days from weak emission at -1.6 and +2.0 MHz from the main line. The continuum has been subtracted.

Fig. 2. (Left) Fits of the average (June 12 + 13, 2015) CO(3-2) line using several temperature profiles and a surface pressure of 12 μ bar. Green and dashed : model calculations with the Dias-Oliveira et al. (2015) profile and CO = 500 ppm. Blue: best fit with a modified temperature profile (shown in blue in right panel) having T = 69 K above 300 km. Red: best fit after simultaneous inversion of CO mole fraction and thermal profile, using the Dias-Oliveira et al. (2015) profile as a priori. (Right): thermal profiles.

Fig. 3. Set of a priori (dashed) and retrieved (solid) temperature profiles, using a surface pressure of 12 μ bar. (Left). CO is fixed at 500 ppm. (Right). CO is retrieved simultaneously (see Table 3 for results). Light blue, black and dark blue curves refer to isothermal a priori profiles at 40, 70 and 100 K, respectively. Red and green curves refer to the temperature profiles of Dias-Oliveira et al. (2015) and Gladstone et al. (2016) as a priori.

Fig 4. Information content of the CO(3-2) line. Averaging kernels at 0 (purple, solid line), 100 (dark blue, dotted), 200 (light-blue, short-dashed), 300 (green, dashed-dot), 500 (yellow, dashed-three dots) and 700 km (red, long-dashed) are shown. They are calculated for the CO, T(z) solution achieved using the Dias-Oliveira et al. (2015) profile as a priori. While kernels at 0, 100, 200 and 300 km peak near the corresponding altitude, kernels at 500 and 700 km peak at 300-350 km, indicating that temperatures at and above 500 km are not determined from the measurements themselves, but rather from the a priori profile and the correlation with the retrieved temperatures at lower altitudes. The solid black line (upper x scale) shows the total kernel as a function of altitude.

Fig. 5. Effect of surface pressure and calibration uncertainty on retrieved thermal profiles. For nominal calibration: p = 12 μ bar (red, solid line), p = 10 μ bar (green, long-dashed), p = 14 μ bar (blue, short-dashed). For p = 12 μ bar, the effect of multiplying data by factors of 1.05 (light blue, dashed-dotted) and 0.95 (pink, dots) is also shown. All profiles are retrieved

using the “mixed” a priori profile (see text) shown in black.

Fig. 6. Manual fits of the HCN (4-3) average (June 12 + 13, 2015) line, using the nominal temperature profile (shown in red in Fig. 5 and here in black in the top right panel), a surface pressure of 12 μ bar, and a variety of HCN distributions, as shown in the bottom right panel. The yellow curve in the bottom right panel is the best fit two-component distribution obtained if the “cold Dias-Oliveira” temperature profile (yellow curve in upper right panel) is used. The yellow and light blue curves are indistinguishable above 450 km.

Fig. 7. Vertical profiles of HCN (solid lines) retrieved from the HCN (4-3) line using a different set of a priori HCN profiles (dashed lines with same color code). The thin dotted line is the saturation profile for the adopted nominal thermal profile. The solid black line marked “Physical” is the HCN vertical profile in the preliminary model of Lavvas et al. (see text). Dashed line: same profile, divided by 2, allowing a match of the HCN line.

Fig. 8. Information content of the HCN(4-3) line. Averaging kernels at 200 (purple, solid line), 400 (dark blue, dotted), 600 (light-blue, short-dashed), 800 (green, dashed-dot), 1000 (yellow, dashed-three dots) and 1200 km (red, long-dashed) are shown. The solid black line (upper x scale) shows the total kernel as a function of altitude. These kernels are calculated for the HCN solution profile returned using a constant HCN = 1×10^{-5} mole fraction as a priori (red curve in Fig. 7).

Fig. 9. Simultaneous fit of CO and HCN line with thermal profiles exhibiting a warm layer and assuming local saturation of HCN at all levels. In the examples shown, the warm layers start 50 km above the mesopause and are 200 km thick. Red, green, and blue curves correspond to mesopause altitudes of 700, 500, and 300 km respectively. The latter case tends to produce an undesired spike in the core of the CO line.

Fig. 10. Upper limits on HC¹⁵N and HC₃N. Top: Average (June 12 + 13, 2015) Pluto spectrum in the region of the HC¹⁵N(4-3) line at 344.200 GHz, compared with models using our preferred HCN distribution (light blue solid line in Fig. 6) and several values of the HC¹⁴N / HC¹⁵N ratio. A lower limit of 125 is indicated by the non-detection of HC¹⁵N. Middle and bottom panels: Average Pluto spectrum in the region of the HC₃N(39-38) and HC₃N(38-37) lines at 354.697 GHz and 345.609 GHz, compared with a

model using the same HCN distribution and a $\text{HC}_3\text{N} / \text{HCN} = 1/10$ ratio.

Fig. 11. New Horizons / Alice line-of-sight (LOS) column densities for CH_4 and N_2 (blue dots, ingress and egress mixed). LOS columns above 850 km for N_2 and 250 km for CH_4 , which are the most reliable, are considered. Data are compared to predictions from a diffusion model with a surface CH_4 mole fraction of 0.65 %, and the eddy K_z and the four temperature profiles shown in the inset. While the nominal profile from this work (black line) matches the Alice data, profiles exhibiting a strong temperature inversion and a ~ 95 K layer in the upper atmosphere (red, green, blue) are at odds with the CH_4 (and N_2 , in general) LOS columns in some parts of the atmosphere.

Fig. 12. Stellar occultation data from July 18, 2012 (VLT/NaCO) (light blue points) are compared with models using the temperature profiles shown in the inset. These include: the “cold Dias-Oliveira” profile (DO15+69 K; black), the standard New Horizons profiles (blue) and three profiles derived from CO line fitting, using different a priori profiles. In the inset, dots indicate the New Horizons/REX measurements (red: immersion, black: emersion). *Upper plots.* Data (normalized stellar flux, ingress and egress folded on each other) and models are plotted vs distance to shadow center. *Lower plots.* Light blue: residuals of the July 18, 2012 data with respect to the best model from Dias-Oliveira et al. (2015). Other curves: residuals of the individual models (with same color coding) with respect to the best model from Dias-Oliveira et al. (2015). All the residuals have been shifted by -0.1 for better clarity.

Fig. 13. Observational thermal profiles from Dias-Oliveira et al. (2015) (yellow), Gladstone et al. (2016, green line) and this work (nominal, black line), are compared to profiles calculated from a radiative-convective model including CH_4 heating/cooling, CO rotational cooling, C_2H_2 vibrational cooling, and HCN rotational cooling for different HCN distributions (dashed lines, upper x scale). Light blue: No HCN. Dark blue: rescaled HCN distribution from Lavvas et al. (in prep.), also shown in Fig. 7, and that allows a match of the HCN line ALMA data. The associated thermal profile never gets colder than ~ 78 K. Red: a much enhanced HCN distribution, that permits an approximate fit of the observed thermal profiles, but at the expense of 20-200 times too high HCN abundances. Calculations from Strobel et al. (in prep.).

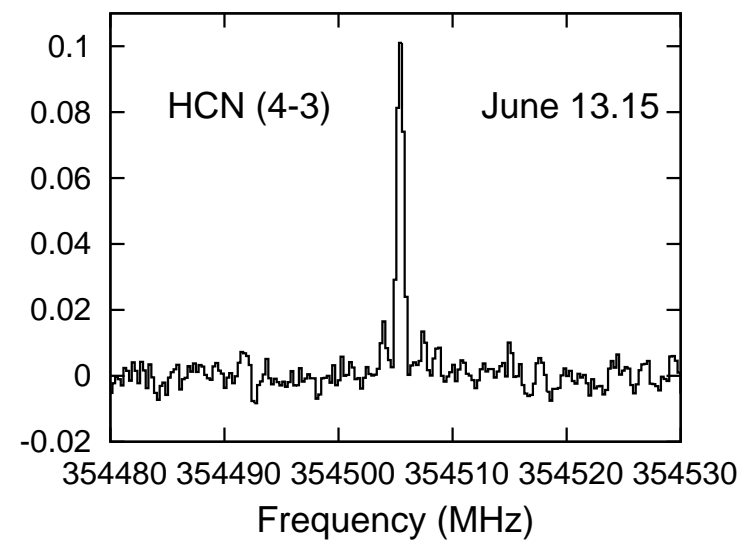
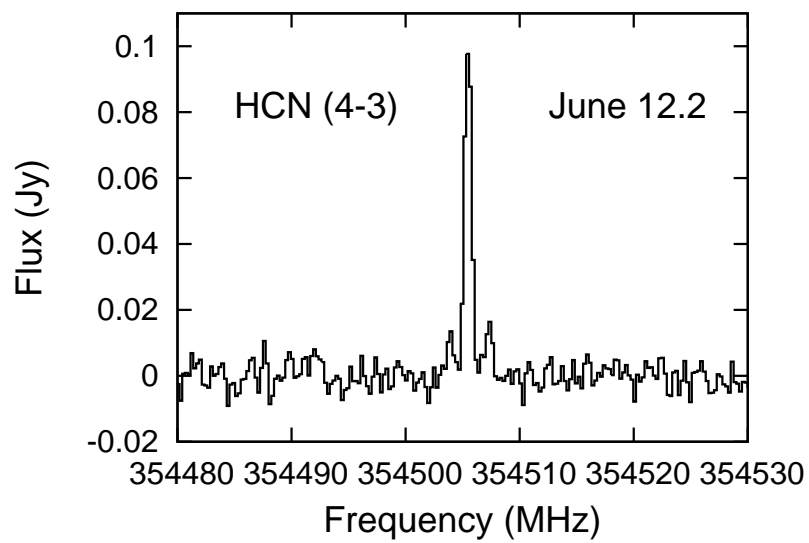
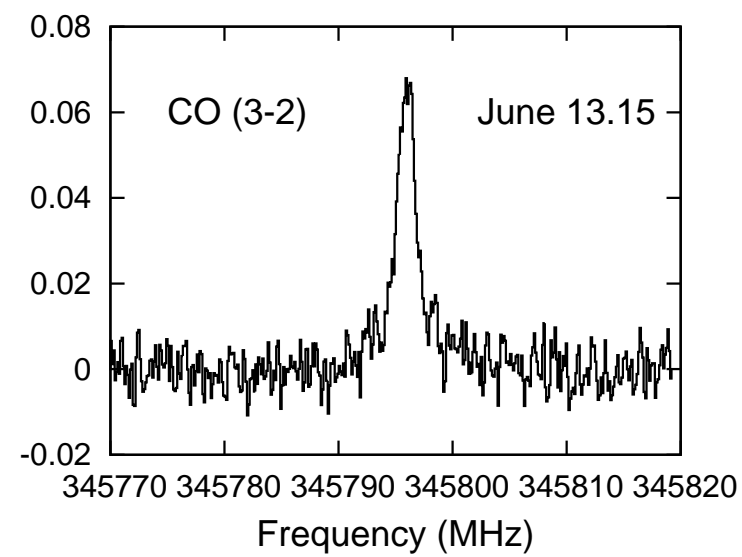
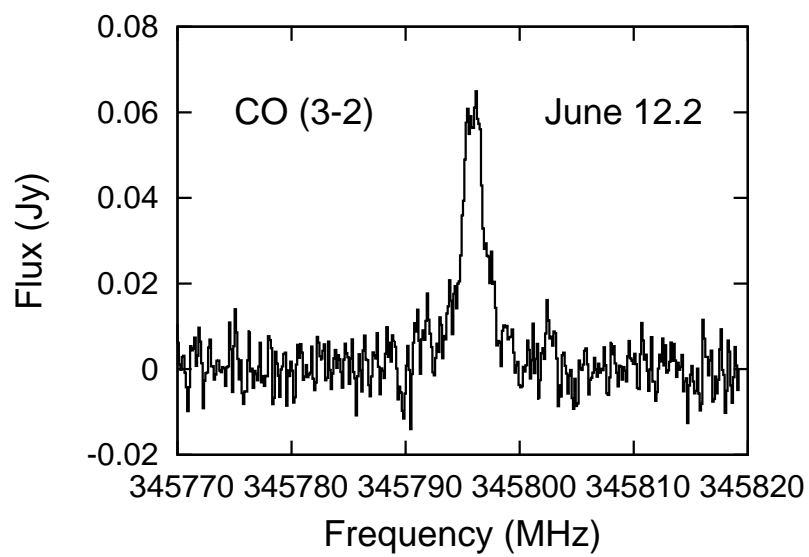


Fig. 1

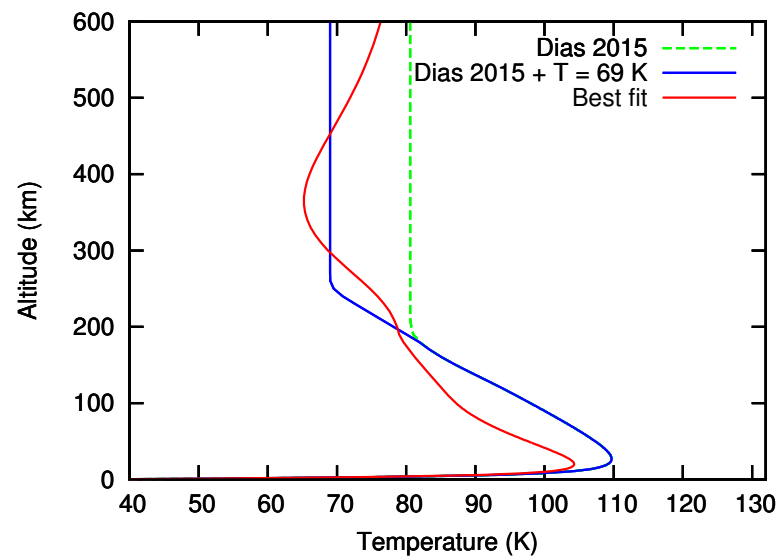
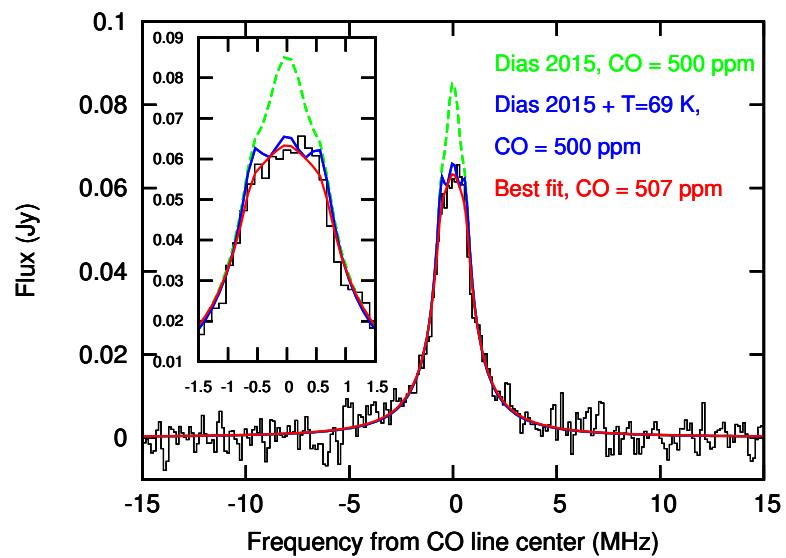


Fig. 2

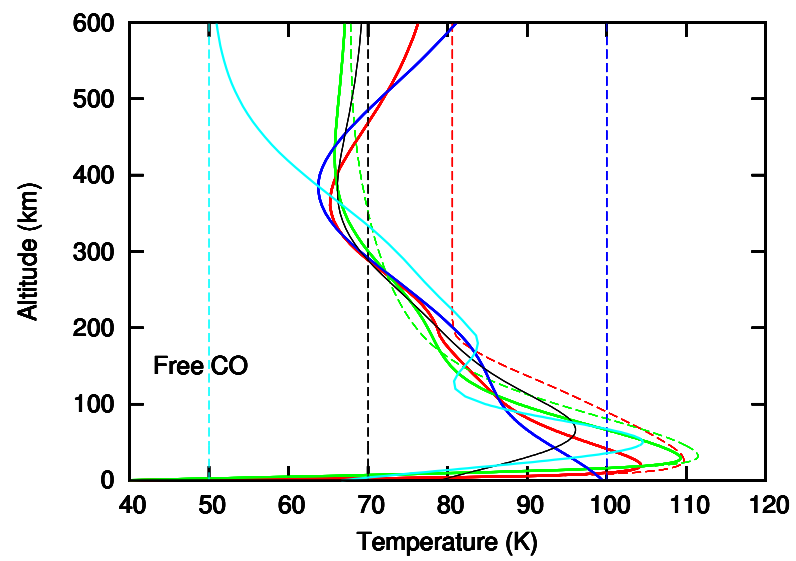
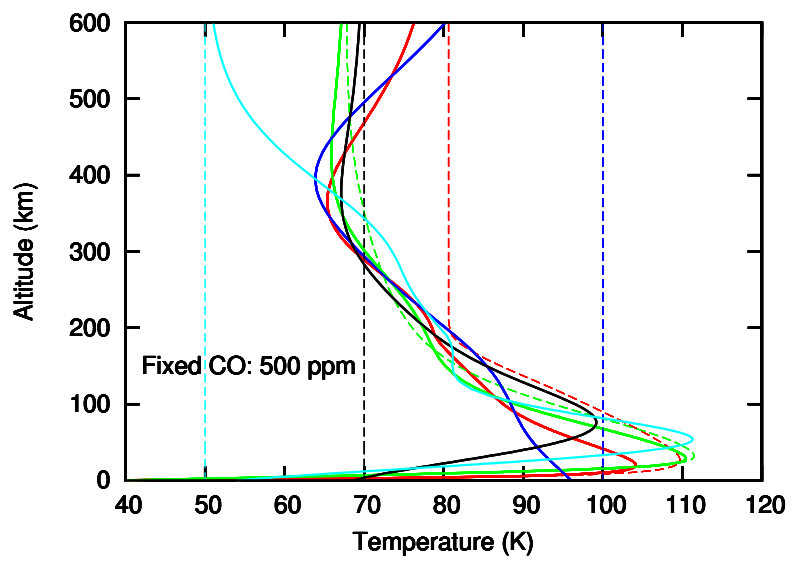


Fig. 3

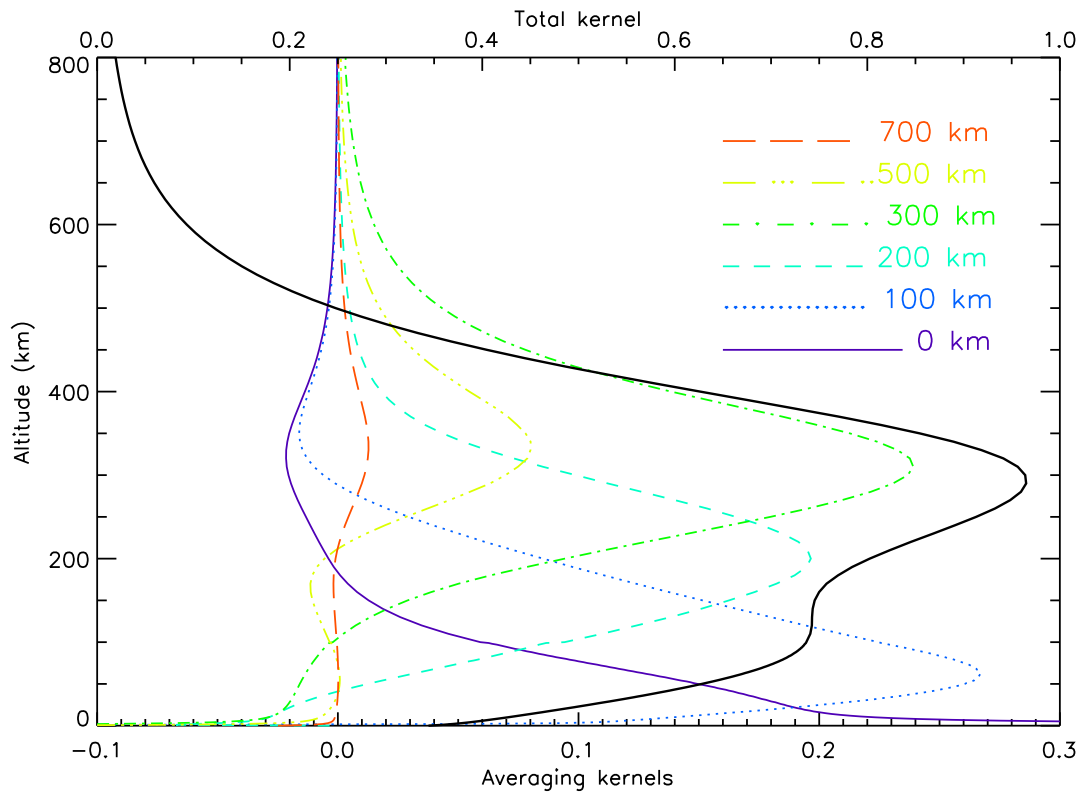


Fig. 4

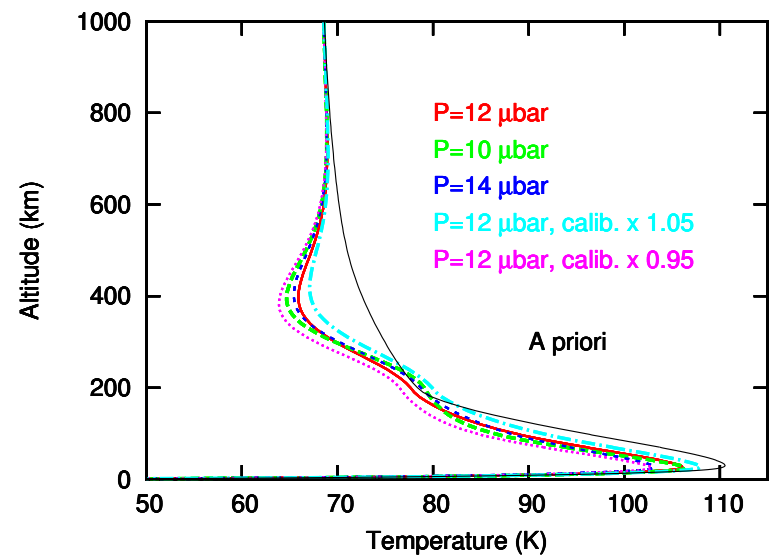
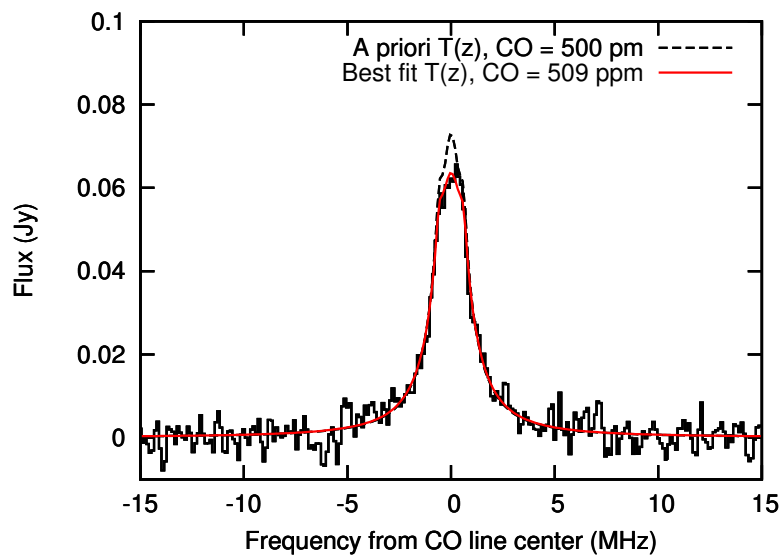


Fig. 5

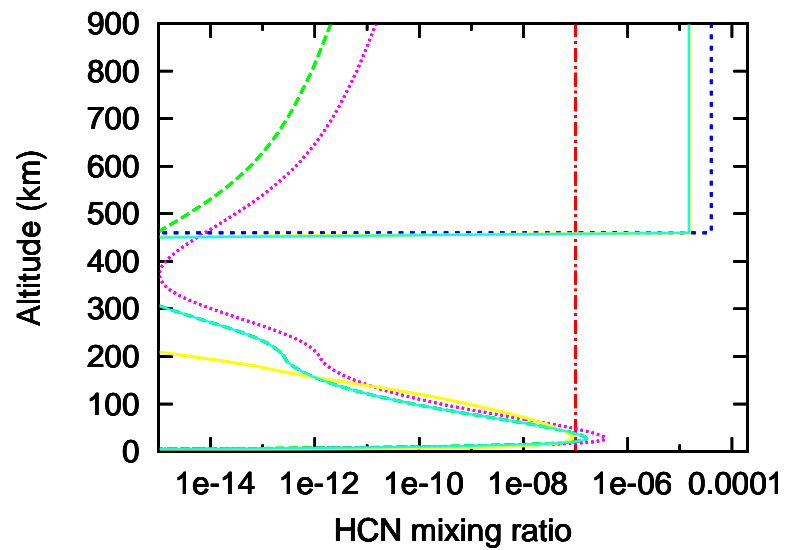
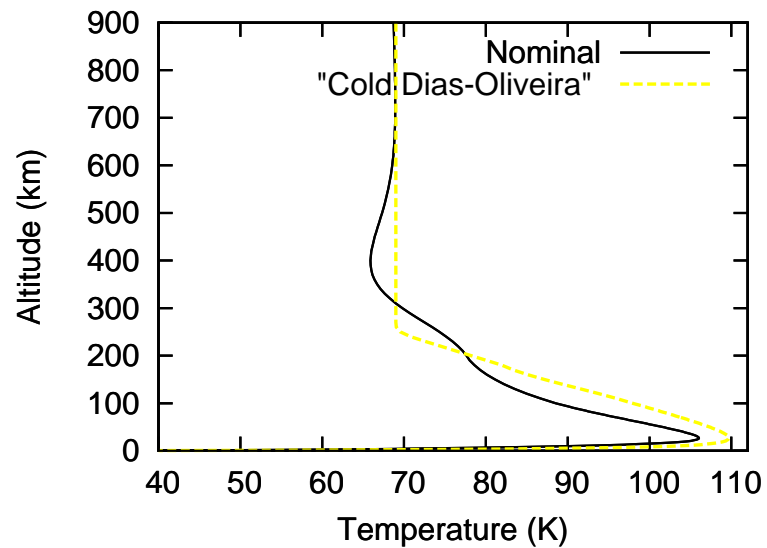
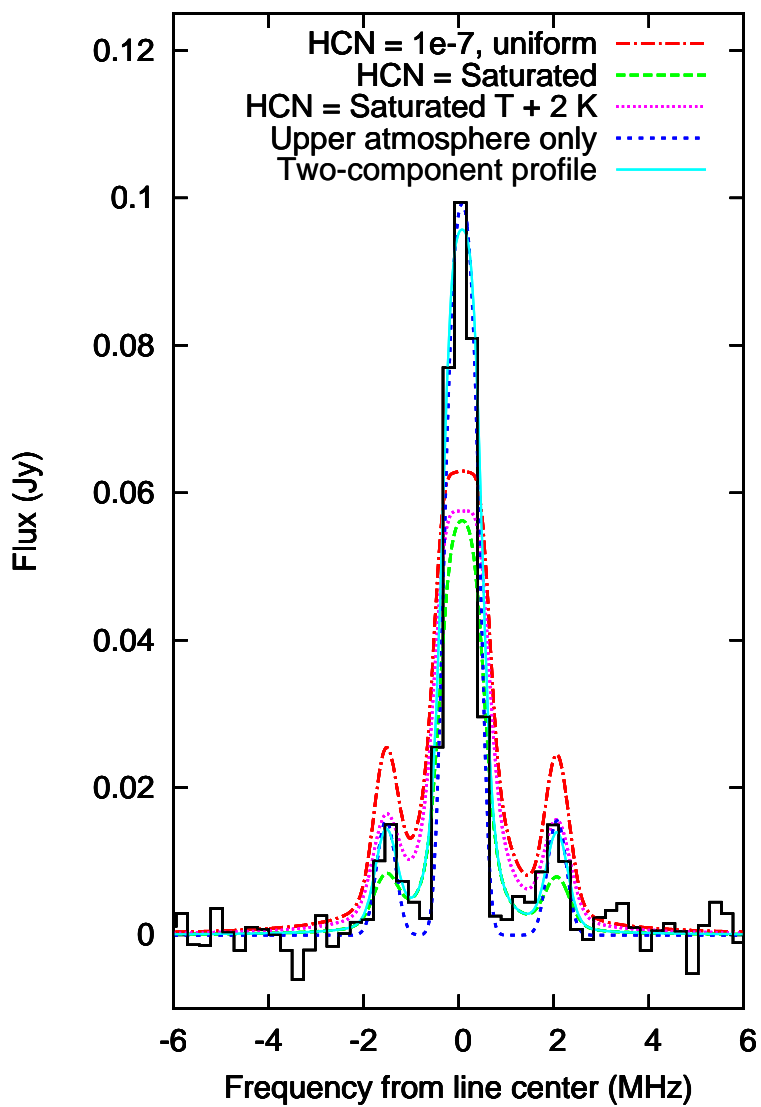


Fig. 6

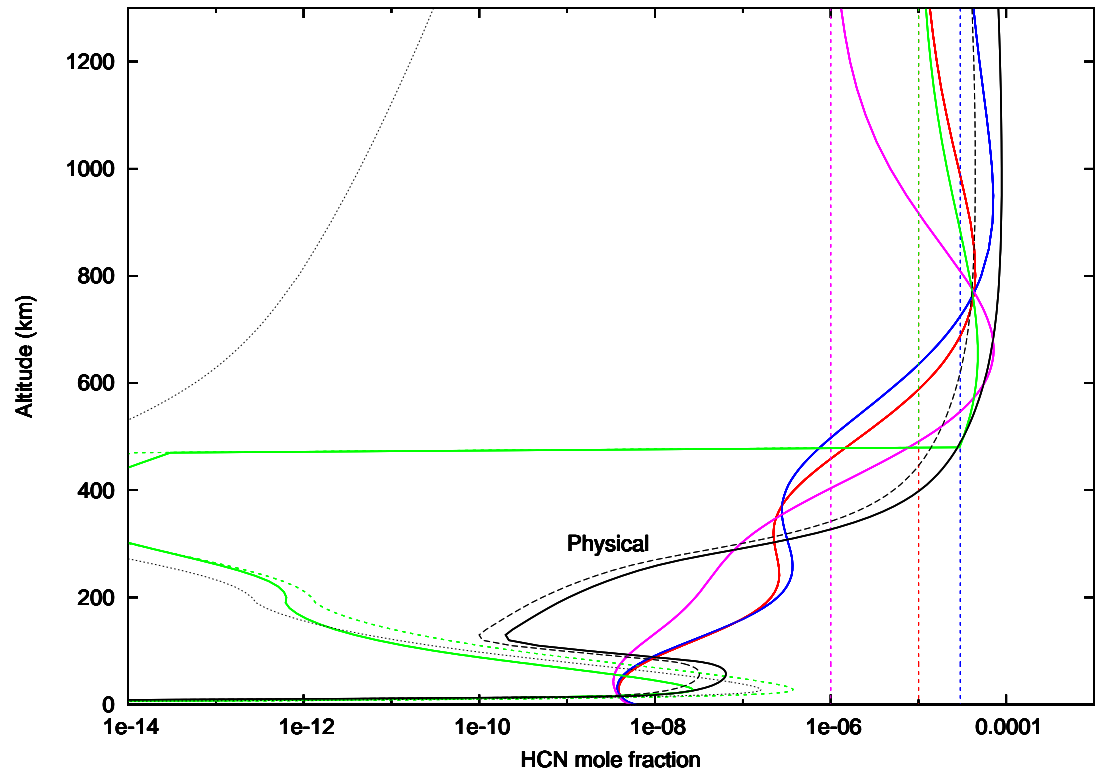


Fig. 7

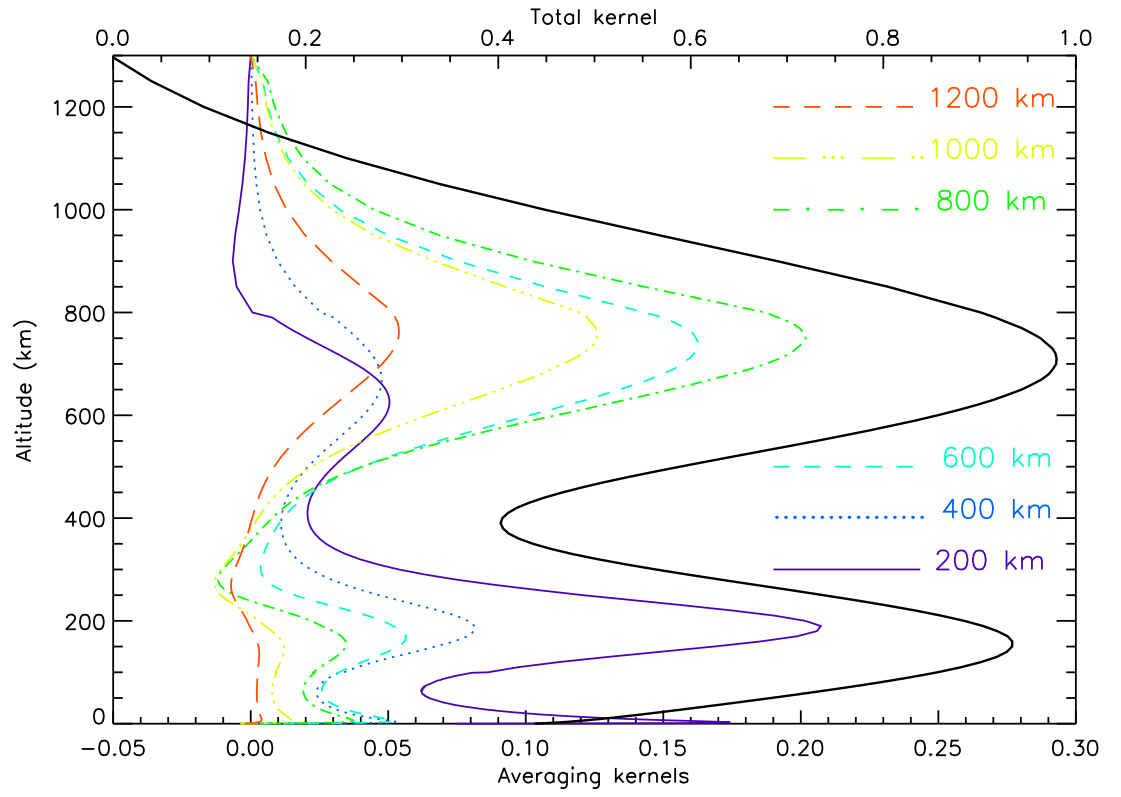


Fig. 8

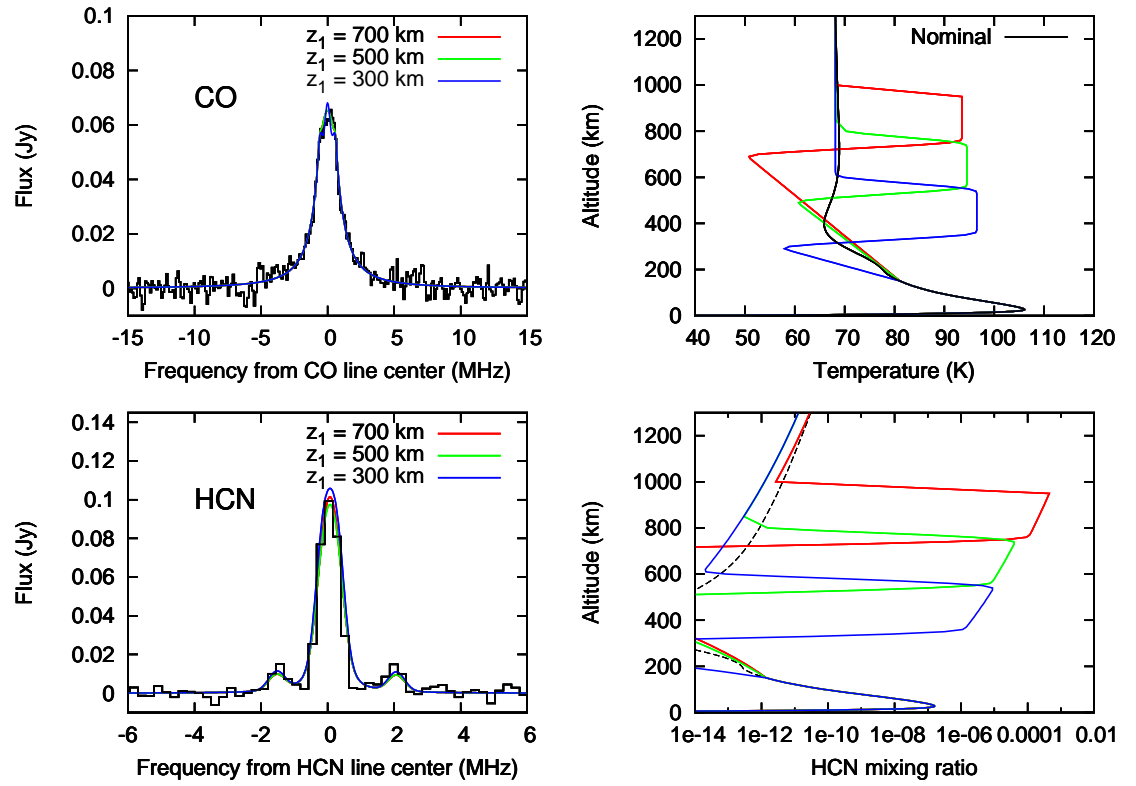


Fig. 9

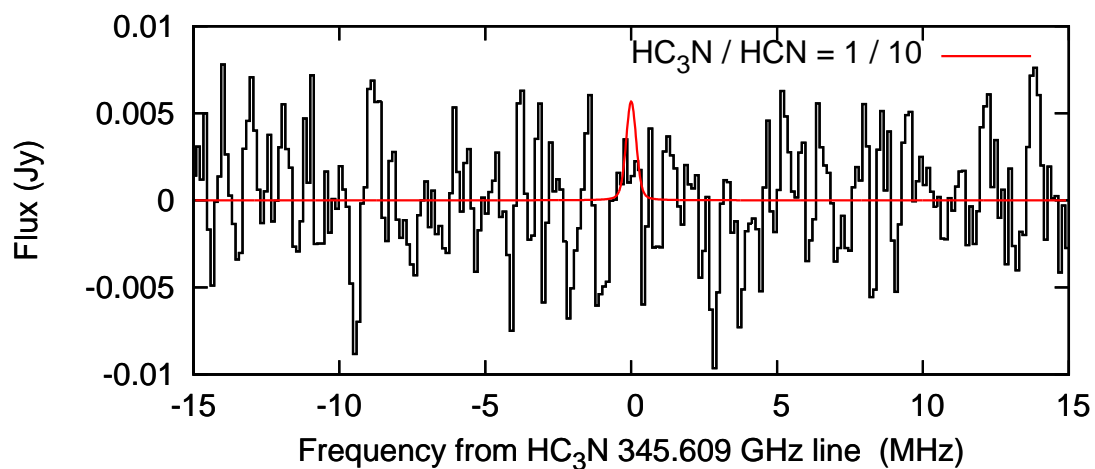
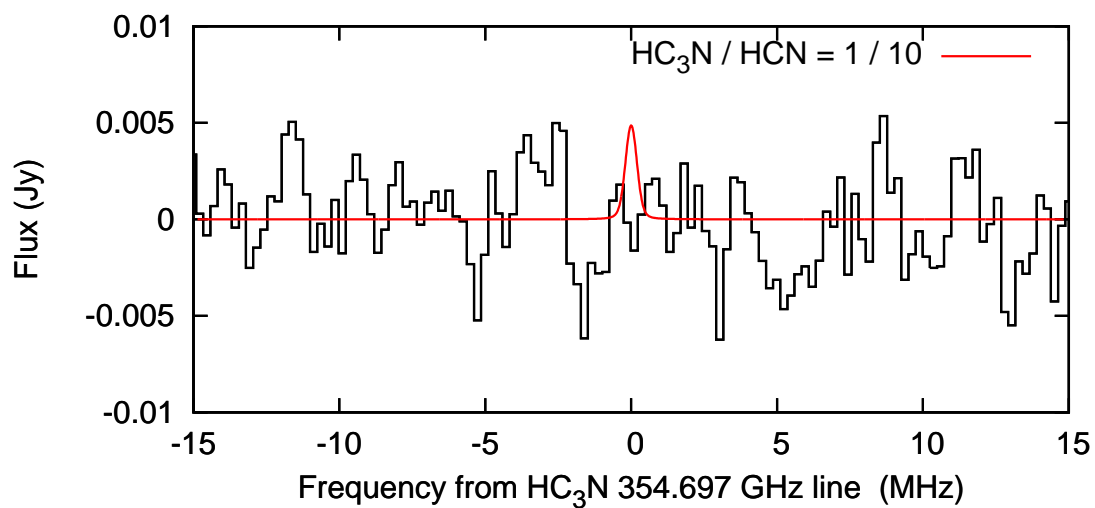
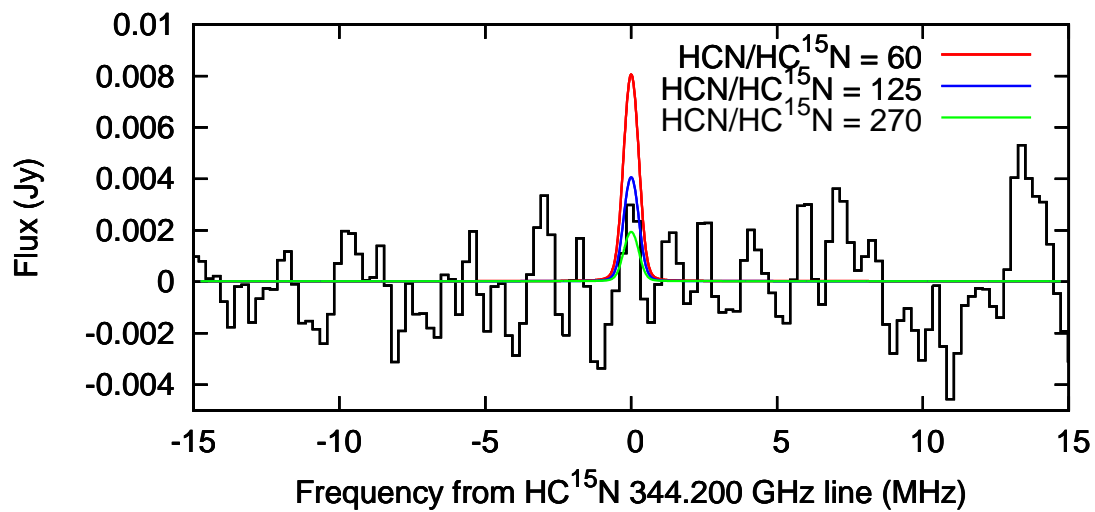


Fig. 10

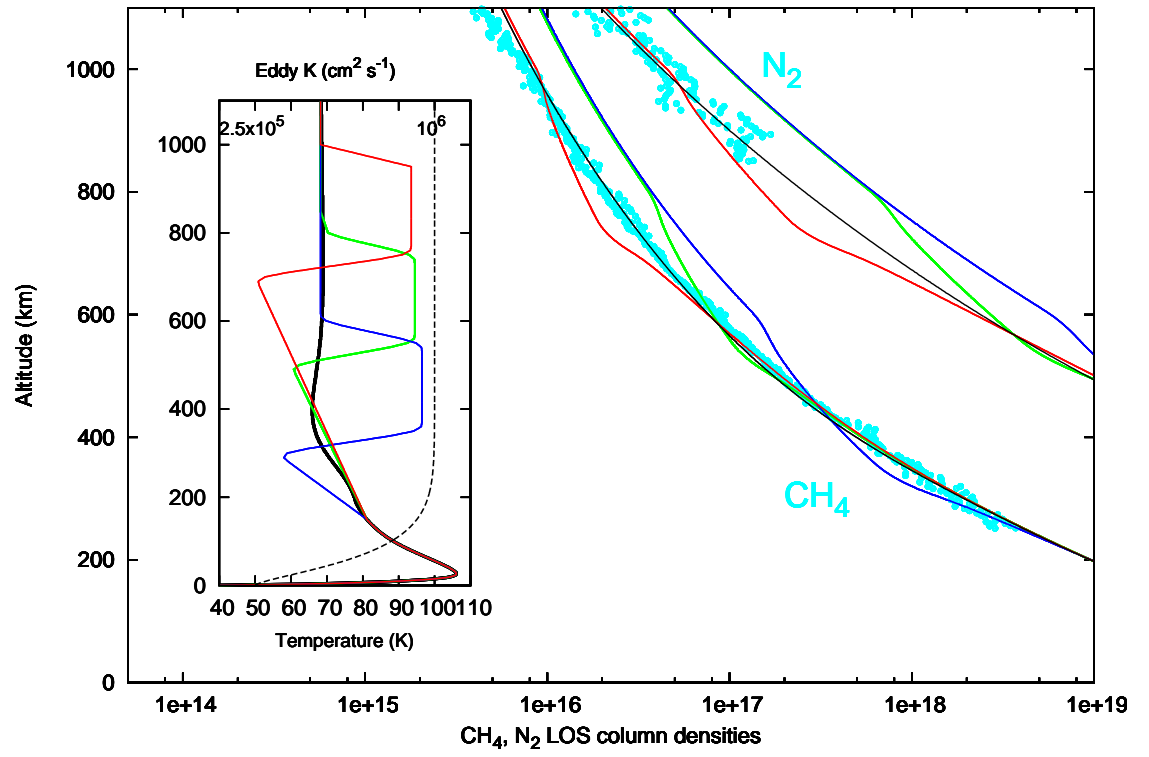


Fig. 11

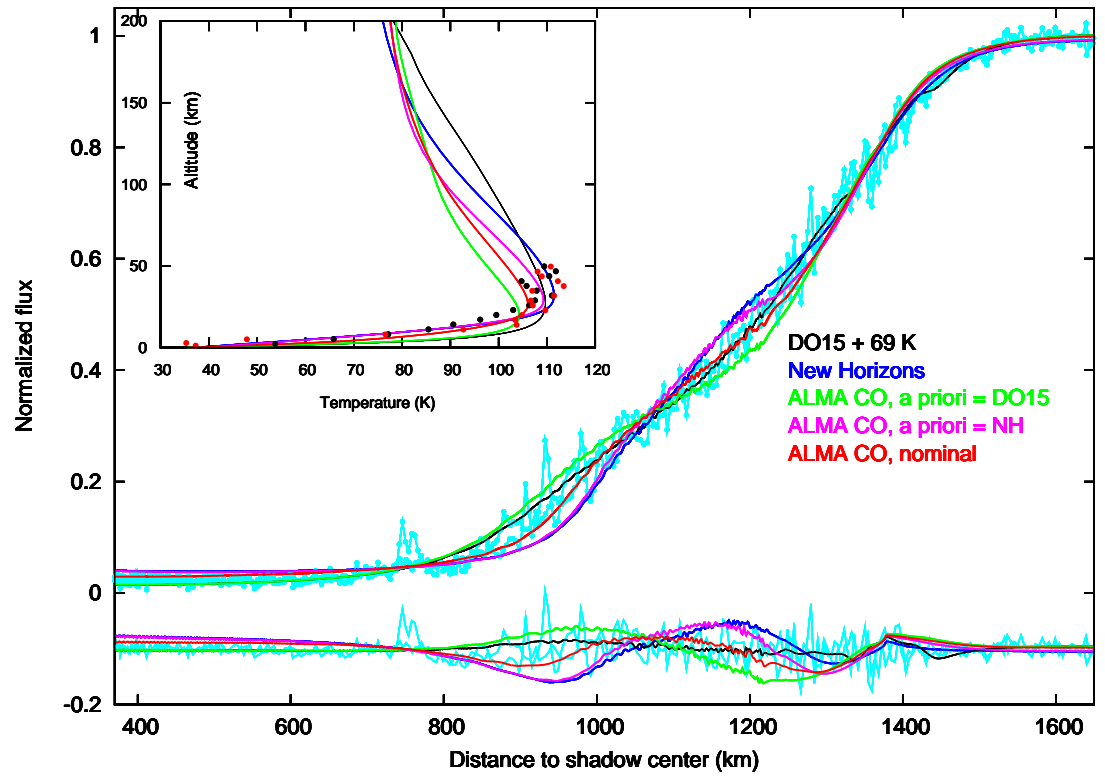


Fig. 12

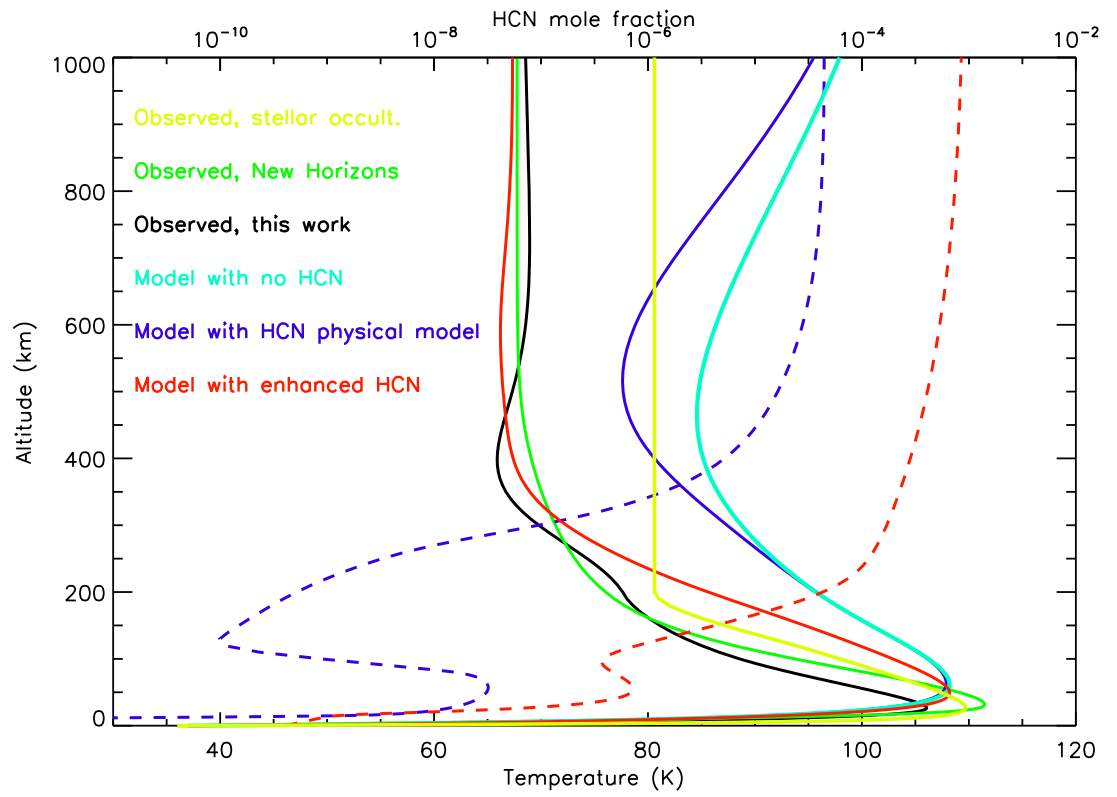


Fig. 13